The Journal of Chemical Physics

Nuclear dynamics in resonant inelastic X-ray scattering and X-ray absorption of methanol

Cite as: J. Chem. Phys. **150**, 234301 (2019); https://doi.org/10.1063/1.5092174
Submitted: 08 February 2019 . Accepted: 24 May 2019 . Published Online: 17 June 2019

Vinícius Vaz da Cruz, Nina Ignatova, Rafael C. Couto, Daniil A. Fedotov, Dirk R. Rehn, Viktoriia Savchenko, Patrick Norman, Hans Ågren, Sergey Polyutov, Johannes Niskanen, Sebastian Eckert, Raphael M. Jay, Mattis Fondell, Thorsten Schmitt, Annette Pietzsch, Alexander Föhlisch, Faris Gel'mukhanov, Michael Odelius, and Victor Kimberg

The Journal of Chemical Physics ARTICLE scitation.org/journal/jcp

Nuclear dynamics in resonant inelastic X-ray scattering and X-ray absorption of methanol

Cite as: J. Chem. Phys. 150, 234301 (2019); doi: 10.1063/1.5092174
Submitted: 8 February 2019 • Accepted: 24 May 2019 •
Published Online: 17 June 2019

Vinícius Vaz da Cruz,[1,2,a] Nina Ignatova,[1,3,4] Rafael C. Couto,[1] Daniil A. Fedotov,[1,3] Dirk R. Rehn,[1] Viktoriia Savchenko,[1,3,4] Patrick Norman,[1] Hans Ågren,[1,5] Sergey Polyutov,[3,4] Johannes Niskanen,[6,7] Sebastian Eckert,[2] Raphael M. Jay,[2] Mattis Fondell,[7] Thorsten Schmitt,[8] Annette Pietzsch,[7] Alexander Föhlisch,[2,7] Faris Gel'mukhanov,[1,3,4] Michael Odelius,[9,b] and Victor Kimberg[1,3,4,c]

AFFILIATIONS

[1]Department of Theoretical Chemistry and Biology, KTH Royal Institute of Technology, 10691 Stockholm, Sweden
[2]Institut für Physik und Astronomie, Universität Potsdam, Karl-Liebknecht-Strasse 24-25, 14476 Potsdam, Germany
[3]Siberian Federal University, 660041 Krasnoyarsk, Russia
[4]Kirensky Institute of Physics, Federal Research Center KSC SB RAS, 660036 Krasnoyarsk, Russia
[5]Department of Physics and Astronomy, Uppsala University, Box 516, SE-751 20 Uppsala, Sweden
[6]Department of Physics and Astronomy, University of Turku, FI-20014 Turun yliopisto, Finland
[7]Institute for Methods and Instrumentation in Synchrotron Radiation Research G-ISRR, Helmholtz-Zentrum Berlin für Materialien und Energie, Albert-Einstein-Strasse 15, 12489 Berlin, Germany
[8]Photon Science Division, Paul Scherrer Institut, CH-5232 Villigen PSI, Switzerland
[9]Department of Physics, Stockholm University, AlbaNova University Center, 10691 Stockholm, Sweden

Note: This paper is part of the JCP special collection on Ultrafast Spectroscopy and Diffraction from XUV to X-ray.

[a]**Electronic mail:** vazdacruz@uni-potsdam.de
[b]**Electronic mail:** odelius@fysik.su.se
[c]**Electronic mail:** kimberg@kth.se

ABSTRACT

We report on a combined theoretical and experimental study of core-excitation spectra of gas and liquid phase methanol as obtained with the use of X-ray absorption spectroscopy (XAS) and resonant inelastic X-ray scattering (RIXS). The electronic transitions are studied with computational methods that include strict and extended second-order algebraic diagrammatic construction [ADC(2) and ADC(2)-x], restricted active space second-order perturbation theory, and time-dependent density functional theory—providing a complete assignment of the near oxygen *K*-edge XAS. We show that multimode nuclear dynamics is of crucial importance for explaining the available experimental XAS and RIXS spectra. The multimode nuclear motion was considered in a recently developed "mixed representation" where dissociative states and highly excited vibrational modes are accurately treated with a time-dependent wave packet technique, while the remaining active vibrational modes are described using Franck–Condon amplitudes. Particular attention is paid to the polarization dependence of RIXS and the effects of the isotopic substitution on the RIXS profile in the case of dissociative core-excited states. Our approach predicts the splitting of the $2a''$ RIXS peak to be due to an interplay between molecular and pseudo-atomic features arising in the course of transitions between dissociative core- and valence-excited states. The dynamical nature of the splitting of the $2a''$ peak in RIXS of liquid methanol near pre-edge core excitation is shown. The theoretical results are in good agreement with our liquid phase measurements and gas phase experimental data available from the literature.

I. INTRODUCTION

Soft X-ray absorption spectroscopy (XAS) and resonant inelastic X-ray scattering (RIXS) are powerful techniques in studies of the molecular electronic structure[1] as they provide insights into the local properties in the vicinity of preselected core-excited atoms in polyatomic systems. Two forms of RIXS are recognized as the final state is either (i) a valence-excited electronic state or (ii) a vibrationally excited state of the electronic ground state in which case the scattering process is also referred to as resonant quasi-elastic X-ray scattering. In particular, the latter form of RIXS can deliver detailed information about the nuclear dynamics and interatomic potentials.[2–4] Extended regions of the ground state potential can be probed since the nuclear wave packet can move far away from the equilibrium in the intermediate state as will be amply demonstrated in the present work. In a combination of XAS and RIXS, we study the electronic and vibrational structures of methanol in the gas phase. Methanol, CH_3OH, is an important compound used in several practical applications such as renewable fuels and hydrogen storage mediums. In addition, CH_3OH is of principal interest because, in its liquid form, it is a system that like water[4–6] is dominated by hydrogen-bond interactions[7–10]—although it is noted that the replacement of a hydrogen by a methyl group in going from water to methanol gives rise to an amphiphilic character of the latter as well as different solvent properties.

The properties of liquid methanol have been thoroughly explored using many different experimental techniques including neutron diffraction,[11] X-ray diffraction,[7,11,12] X-ray emission spectroscopy (XES),[13] XAS,[14] and RIXS.[15] In the theoretical part of our study, we focus on methanol in the gas phase and on providing an accurate assignment of the associated XAS and RIXS spectra at the oxygen K-edge, as available from the literature.[16–18] Our study is motivated by the lack of a comprehensive theoretical study of the X-ray spectra of this system and will serve as an important stepping stone to understand the corresponding spectra in the liquid phase that are obtained in the present work. The O1s X-ray absorption spectra of gas phase methanol were investigated by different groups.[16–18] Usually, the assignment of the O1s pre-edge XAS spectrum is made by means of calculations based on semiempirical methods,[16–18] but an exception is found in Ref. 14 where the transition-potential density functional theory (TP-DFT) approach was adopted. However, the TP-DFT is not truly a method based on first-principles as, most notably, the charge of the core hole in the creation of the transition potential functions in practice is a spectral tuning parameter and, furthermore, a detailed spectral assignment is absent in this article. Therefore, the first aim of our study is to shed light on the electronic core-excited states which form the pre-edge XAS of gas phase methanol using high-level *ab initio* quantum chemical calculations.[19–22] Another shortcoming of most previous studies is the neglect of nuclear quantum dynamics although it was demonstrated through the RIXS measurements in gas phase methanol[18] and in the liquid phase[15] that there is a strong sensitivity of the high-energy RIXS peak to isotopic substitution. This observation makes it timely to investigate the role of nuclear dynamics in both XAS and RIXS spectra of this important system. The developed theoretical approach used in our simulations of nuclear dynamics in methanol is similar to the one used in our earlier studies of the RIXS spectrum of water[23–26] with the key difference being the treatment of a larger number of normal modes.

The paper is organized as follows. In Sec. II, we outline the multimode theory of XAS and RIXS, using a so-called mixed representation. The computational methods are described in Sec. III. In Sec. IV A, we present the results of calculations of the XAS spectrum. In Sec. IV B, we start the study of RIXS by considering the quasi-elastic channel. In Sec. IV C, we discuss the pseudo-atomic band and the role of isotopic substitution on the RIXS profile. In Sec. IV D, we present the results of simulations of RIXS for different final and core-excited states taking into account only the electronic degrees of freedom. Finally, in Sec. IV E, we discuss the RIXS process in liquid methanol. Our findings are summarized in Sec. V.

II. THEORY AND METHODOLOGY

A. Time-dependent picture

We study the RIXS process starting from the multimode vibrational state of the ground state, characterized by the vector of vibrational quantum numbers $v_0 = (v_0^{(0)}, v_0^{(1)}, v_0^{(2)}, \cdots)$, and ending up in the multimode vibrational state $v_f = (v_f^{(0)}, v_f^{(1)}, v_f^{(2)}, \cdots)$ of the final electronic state. We adopt the time-dependent representation for the XAS $\sigma_{\rm abs}(\omega)$ and RIXS $\sigma(\omega', \omega)$ cross sections,[24,27,28]

$$\begin{aligned}
\sigma_{\rm abs}(\omega) &= {\rm Re}\sum_c \langle v_0|\tilde{\Psi}(0)\rangle,\\
\sigma(\omega',\omega) &= \frac{1}{\pi}{\rm Re}\int_0^\infty e^{\imath(\omega-\omega'-\omega_{f0}+\varepsilon_{v_0}+\imath\Gamma_f)t}\sigma(t)dt,\\
\sigma(t) &= \langle\Psi(0)|\Psi(t)\rangle,\\
|\Psi(0)\rangle\!\rangle &= \imath\sum_{v_c}\frac{D_{fc}|v_c\rangle\langle v_c|D_{c0}|v_0\rangle}{\omega-\omega_{c0}+\varepsilon_{v_0}-\varepsilon_{v_c}+\imath\Gamma}\\
&= D_{fc}\int_0^\infty e^{\imath(\omega-\omega_{c0}+\varepsilon_{v_0}+\imath\Gamma)t}|\psi_c(t)\rangle\!\rangle dt,
\end{aligned} \tag{1}$$

where the wave packet $\tilde{\Psi}(0)$ is given by the same equation as $\Psi(0)$ except that both $D_{fc} = (\mathbf{e}'\cdot\mathbf{d}_{fc})$ and $D_{c0} = (\mathbf{e}\cdot\mathbf{d}_{c0})$ should be replaced by $\mathbf{d}_{c0}$. The RIXS process with the scattering amplitude $F_{v_f} = -\imath\langle v_f|\Psi(0)\rangle\!\rangle$ is affected by nuclear dynamics in the core-excited state and in the final (ground) state as represented in the nuclear wave packets

$$|\psi_c(t)\rangle\!\rangle = e^{-\imath h_c t}D_{c0}|v_0\rangle, \quad |\Psi(t)\rangle\!\rangle = e^{-\imath h_f t}|\Psi(0)\rangle\!\rangle. \tag{2}$$

Here $(\omega, \mathbf{e})$ and $(\omega', \mathbf{e}')$ are the frequencies and polarization vectors of incoming and scattered photons, respectively; ω_{ij} is the spacing between minima of the potential energy surfaces of the electronic states i and j, with $i, j = 0, c, f$ denoting the ground 0, core-excited c, and final f electronic states, respectively; Γ and Γ_f are the lifetime broadenings of the core-excited and final states, respectively. Note that throughout the text, Γ refers to the half-width at half-maximum (HWHM) value. The transition amplitudes $D_{fc} = (\mathbf{e}'\cdot\mathbf{d}_{fc})$ and $D_{c0} = (\mathbf{e}\cdot\mathbf{d}_{c0})$ depend on the scalar product of polarization vectors and corresponding dipole moments of electronic transitions. In the simulations, we employ the Born–Oppenheimer (BO)

approximation, assuming a small influence of coupling between dynamics in different excited states.

B. Mixed representation and the mD + nD model

It is quite common in electronically excited states that some degrees of freedom are dissociative or excited above the dissociation limit. They require special treatment due to the continuity of the vibrational spectrum.[23,24,26] The best numerical method for continuum states is the time-dependent wave packet technique.[27,28] Since degrees of freedom which have bound potentials can be treated more efficiently in the frequency domain, we will use a mixed representation for the cross section. The m modes will be described using the time-dependent wave packet technique, while the remaining n modes are treated using the stationary method of Franck–Condon (FC) amplitudes. Let us write the total nuclear Hamiltonian as a sum of two independent terms,

$$h_i = h_i^{(m)} + h_i^{(n)}, \quad i = 0, c, f, \tag{3}$$

neglecting the coupling between the selected subspaces of vibrational modes. We will look for the solution of the Schrödinger equation with the Hamiltonian h_i in the mixed (time-energy) representation as the product of wave packet $\psi_i^{(m)}(t)$ and eigenfunction $|\nu_i\rangle = |\nu_i^{(1)}, \nu_i^{(2)}, \cdots \nu_i^{(n)}\rangle$,

$$\begin{aligned} &|\psi_i^{(m)}(t)\rangle|\nu_i\rangle, \\ &\imath\frac{\partial}{\partial t}|\psi_i^{(m)}\rangle = h_i^{(m)}|\psi_i^{(m)}\rangle, \\ &h_i^{(n)}|\nu_i\rangle = \varepsilon_{\nu_i}|\nu_i\rangle. \end{aligned} \tag{4}$$

The m degrees of freedom are described in the time domain, while the stationary Schrödinger equation is used for the rest of the n modes $|\nu_i\rangle$. Consequently, the initial vibrational state in general Eq. (2) should be replaced as follows:

$$|\nu_0\rangle \to |\mu_0\rangle|\nu_0\rangle, \quad \varepsilon_{\nu_0} \to \varepsilon_{\mu_0} + \varepsilon_{\nu_0}. \tag{5}$$

Here $(|\mu_0\rangle, \varepsilon_{\mu_0})$ and $(|\nu_0\rangle, \varepsilon_{\nu_0})$ are the eigenfunctions and eigenvalues of the ground state Hamiltonians $h_0^{(m)}$ and $h_0^{(n)}$, respectively. Using a condition of completeness, $1 = \sum|\nu_c\rangle\langle\nu_c|$, and $\exp(-\imath h_i t) = \exp(-\imath h_i^{(n)} t)\exp(-\imath h_i^{(m)} t)$, one can get the following expression for the wave packet in Eq. (2):

$$\begin{aligned} |\psi_c(t)\rangle &= e^{-\imath h_c^{(n)} t}|\nu_0\rangle e^{-\imath h_c^{(m)} t} D_{c0}|\mu_0\rangle = \sum_{\nu_c} e^{-\imath\varepsilon_{\nu_c} t}|\nu_c\rangle\langle\nu_c|\nu_0\rangle|\psi_c^{(m)}(t)\rangle, \\ |\psi_c^{(m)}(t)\rangle &= e^{-\imath h_c^{(m)} t} D_{c0}|\mu_0\rangle. \end{aligned} \tag{6}$$

Now, we are at liberty to rewrite the expression for the wave packet $|\Psi(0)\rangle$ in Eq. (1),

$$\begin{aligned} |\Psi(0)\rangle &= \sum_{\nu_c}|\nu_c\rangle\langle\nu_c|\nu_0\rangle|\Psi_{\nu_c}(0)\rangle, \\ |\Psi_{\nu_c}(0)\rangle &= D_{fc}\int_0^\infty e^{\imath(\omega-\omega_{c0}+\varepsilon_{\nu_0}+\varepsilon_{\mu_0}-\varepsilon_{\nu_c}+\imath\Gamma)t}|\psi_c^{(m)}(t)\rangle dt, \end{aligned} \tag{7}$$

and for the wave packet $|\Psi(t)\rangle$, we get

$$\begin{aligned} |\Psi(t)\rangle &= e^{-\imath h_f^{(n)} t} e^{-\imath h_f^{(m)} t}\sum_{\nu_c}|\nu_c\rangle\langle\nu_c|\nu_0\rangle|\Psi_{\nu_c}(0)\rangle \\ &= \sum_{\nu_f}\sum_{\nu_c} e^{-\imath\varepsilon_{\nu_f} t}|\nu_f\rangle\langle\nu_f|\nu_c\rangle\langle\nu_c|\nu_0\rangle|\Psi_{\nu_c}(t)\rangle, \\ \Psi_{\nu_c}(t) &= e^{-\imath h_f^{(m)} t}\Psi_{\nu_c}(0). \end{aligned} \tag{8}$$

Here, we used the expression in Eq. (7) for $|\Psi(0)\rangle$ and the condition of the completeness $1 = \sum|\nu_f\rangle\langle\nu_f|$. Using the orthonormality of the vibrational states $\langle\nu_f|\nu_f'\rangle = \delta_{\nu_f,\nu_f'}$ and the insertion of Eqs. (7) and (8) into Eq. (1), one can compute the autocorrelation function $\sigma(t)$ in Eq. (1). This allows us to formulate the employed expression for the RIXS cross section in the mixed (mD + nD) representation

$$\begin{aligned} \sigma_{\text{abs}}(\omega) &= \text{Re}\sum_{\nu_c}|\langle\nu_0|\nu_c\rangle|^2\langle\mu_0|\tilde{\Psi}_{\nu_c}(0)\rangle, \\ \sigma(\omega',\omega) &= \frac{1}{\pi}\text{Re}\sum_{\nu_f\nu_c'\nu_c}\langle\nu_0|\nu_c'\rangle\langle\nu_c'|\nu_f\rangle\langle\nu_f|\nu_c\rangle\langle\nu_c|\nu_0\rangle \\ &\quad\times\int_0^\infty e^{\imath(\omega-\omega'-\omega_{f0}-\varepsilon_{\nu_f}+\varepsilon_{\nu_0}+\varepsilon_{\mu_0}+\imath\Gamma_f)t}\sigma_{\nu_c'\nu_c}(t)dt, \\ \sigma_{\nu_c'\nu_c}(t) &= \langle\Psi_{\nu_c'}(0)|\Psi_{\nu_c}(t)\rangle, \end{aligned} \tag{9}$$

where $\tilde{\Psi}_{\nu_c}(0)$ is defined similarly as $\tilde{\Psi}(0)$ [see Eq. (1)].

C. Polarization dependence

In the current study, we will ignore the change in the transition dipole moment during the course of nuclear motion and we use the equilibrium values for $\mathbf{d}_{c0}$ and $\mathbf{d}_{fc}$. Since we explore the XAS and RIXS spectra of gas phase methanol, the cross sections should be averaged over isotropic molecular orientations using equations[28,29] $\overline{(\mathbf{e}\cdot\mathbf{d}_{c0})^2} = \mathrm{d}_{c0}^2/3$ and

$$\begin{aligned} &\overline{(\mathbf{e}\cdot\mathbf{d}_{c0})(\mathbf{e}\cdot\mathbf{d}_{c0})(\mathbf{e}'\cdot\mathbf{d}_{fc})(\mathbf{e}'\cdot\mathbf{d}_{fc})} \\ &\quad= \frac{\mathrm{d}_{c0}^2\mathrm{d}_{fc}^2}{30}\left[3+\cos^2\chi+(1-3\cos^2\chi)(\hat{\mathbf{d}}_{fc}\cdot\hat{\mathbf{d}}_{c0})^2\right], \end{aligned} \tag{10}$$

where $\chi = \angle(\mathbf{e},\mathbf{k}')$ is the angle between polarization vector of incoming photon and momentum of outgoing one and $\hat{\mathbf{d}} = \mathbf{d}/d$ is the unit vector along $\mathbf{d}$. To illustrate the role of polarization, let us consider a core-excitation to a state of A' symmetry, with the transition dipole moment $\mathbf{d}_{\mathscr{A}'}$, and de-excitation to final states of A' or A'' symmetry, with decay transition dipole moments $\mathbf{d}_{A'}$ and $\mathbf{d}_{A''}$, respectively. Taking into account that the transition dipole moments to the states of A' and A'' symmetry are orthogonal, $(\mathbf{d}_{\mathscr{A}'}\cdot\mathbf{d}_{A''}) = 0$, we get

$$\begin{aligned} \sigma_{\mathscr{A}'A''} &\propto \mathrm{d}_{\mathscr{A}'}^2\mathrm{d}_{A''}^2(3+\cos^2\chi), \\ \sigma_{\mathscr{A}'A'} &\propto \mathrm{d}_{\mathscr{A}'}^2\mathrm{d}_{A'}^2\left[3+\cos^2\chi+(1-3\cos^2\chi)(\hat{\mathbf{d}}_{\mathscr{A}'}\cdot\hat{\mathbf{d}}_{A'})^2\right]. \end{aligned} \tag{11}$$

Bear in mind that the transition dipole moments $\mathbf{d}_{\mathscr{A}'}$ and $\mathbf{d}_{A'}$ are not necessarily parallel to each other despite that both lie in the symmetry plane of the equilibrium geometry.

D. Electronic structure theory calculations

The ground-state electronic configuration of methanol is $(1a')^2$, $(2a')^2$, $(3a')^2$, $(4a')^2$, $(1a'')^2$, $(5a')^2$, $(6a')^2$, $(7a')^2$, and $(2a'')^2$, where the $1a'$-orbital is the atomic oxygen 1*s*-orbital. To shed light on the electronic structure of the methanol molecule in the ground state and the O1s core-excited states, it is useful to consider the natural orbitals. Figure 1 shows the occupied natural orbitals which we obtained from the restricted active space self-consistent field (RASSCF)[30] calculation (see Sec. III) of the ground state. The unoccupied natural orbitals $\phi_i = 8a', 9a', 3a'', 10a', 11a'$, and $12a'$ are obtained from separate calculations for each core-excited state $|\Phi_i\rangle = |1a'^{-1}\phi_i\rangle$, where $1s_O = 1a'$. Despite the fact that we use multiconfigurational approaches, we adopt, for brevity, a one-electron $|1a'^{-1}\phi_i\rangle$ notation for the total wavefunction. Thereby, we specify the largest contribution in the multi-electron wave function $|\Phi_i\rangle$, where the occupation number of the natural orbital ϕ_i exceeds 90%. Hence, we assign the singlet core-excited states according to the orbital which is unoccupied in the ground state and receives the core-electron in the course of photoabsorption. We use the capital letters for multi-electron states to distinguish them from one-electron orbitals in lowercase letters,

$$|8\mathscr{A}'\rangle = |1a'^{-1}8a'^{1}\rangle, \quad |9\mathscr{A}'\rangle = |1a'^{-1}9a'^{1}\rangle, \\ |3\mathscr{A}''\rangle = |1a'^{-1}3a''^{1}\rangle, \cdots. \tag{12}$$

The same notation for the multi-electron states is used in the single-reference propagator-based calculations of the excited states, but the excitation vectors (the eigenvectors of the respective secular equation) refer in these cases to canonical Hartree–Fock or Kohn–Sham orbitals.

Underlying the simulations of nuclear dynamics as described above, we performed limited scans of the potential energy surfaces of the electronic ground state and the low-lying oxygen core-excited states. Prior to addressing the excited states, we determined the global minimum of the electronic ground state and found the associated normal mode coordinates along which we explored the potentials of the collection of electronic states involved in the XAS and RIXS processes. The DFT method is widely employed to determine ground state molecular structures and vibrational frequencies of polyatomic systems with reliable agreement to the experiment and we adhere to this choice (see Sec. III for details). For instance, the vibrational frequencies of methanol as here obtained with the B3LYP hybrid functional[31,32] display an agreement with the experiment results reported in Ref. 33 that exceeds what is found at the complete active space second order perturbation theory (CASPT2) framework;[19,20] see Table I. Relying on the results of the normal mode analysis, we constructed the 1D potential energy curves (PECs) along the corresponding normal modes obtained with the DFT method, as described in Sec. III. The subsequent simulations of the XAS and RIXS spectra were performed in the framework of the (1D + 3D)-model neglecting mode couplings, as described in further detail in Sec. IV A 2.

In particular, for unbound core-excited states, the time-dependent wave packet approach will probe the PECs far away from the equilibrium and we therefore use the multireference RAS model for their construction with active spaces adequate to correctly treat the dissociation limit. The core-excited states are all constructed with a common set of orbitals by means of the technique of state-averaging, and these states are thus internally orthogonal, but they are nonorthogonal to and interacting with the ground state. This aspect is an artifact of the approach that in principle makes a calculation of transition properties gauge-origin dependent but which in practice is of minor concern for core-excited states and also handled with the RAS-state interaction (RASSI) approach.[34,35] The main advantage with a separate-state (averaged or not) optimization of core-excited states is the very efficient treatment of the electronic relaxation.

In a propagator or response theory approach, the core-excited states are only indirectly referenced by the solving of secular equations in the frequency-domain and after introducing the core-valence separation (CVS) approximation.[36,37] With this approach,

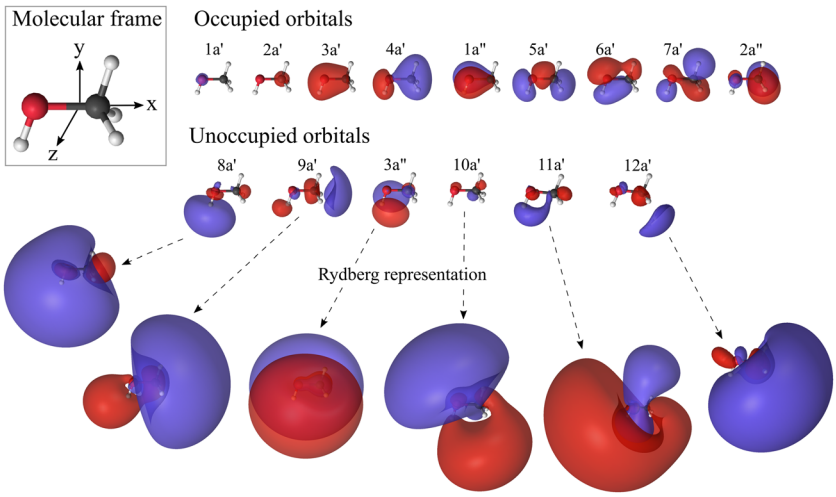

FIG. 1. Occupied natural orbitals are extracted from the ground state multi-electron wavefunction. Unoccupied natural orbitals are extracted from the corresponding state-specific RASSCF calculations of the core-excited states of A' and A'' symmetry. The coordinate system in the molecular frame is shown in the inset of the figure.

TABLE I. Experimental[33] and theoretical (DFT) frequencies of vibrational modes of methanol in the ground state.

Vibrational mode		Sym.	Expt., cm^{-1} (eV)	Theor. (DFT), cm^{-1} (eV)	Theor. (CASPT2), cm^{-1} (eV)
Torsion	ν_{12}	A'	295 (0.036)	296 (0.037)	301 (0.037)
CO stretching	ν_8	A'	1033 (0.128)	1039 (0.129)	1060 (0.131)
CH_3 rock	ν_7	A'	1060 (0.131)	1076 (0.133)	1093 (0.136)
CH_3 rock	ν_{11}	A''	1165 (0.144)	1170 (0.145)	1188 (0.147)
OH bending	ν_6	A'	1345 (0.167)	1365 (0.169)	1375 (0.170)
CH_3 s-deform.	ν_5	A'	1455 (0.180)	1477 (0.183)	1492 (0.185)
CH bending	ν_{10}	A''	1465 (0.182)	1498 (0.186)	1523 (0.188)
CH bending	ν_4	A'	1477 (0.183)	1508 (0.187)	1533 (0.190)
CH stretching	ν_3	A'	2844 (0.353)	2994 (0.371)	3054 (0.378)
CH stretching	ν_9	A''	2960 (0.367)	3040 (0.377)	3131 (0.388)
CH_3 d-stretching	ν_2	A'	3000 (0.372)	3109 (0.385)	3189 (0.395)
OH stretching	ν_1	A'	3681 (0.456)	3829 (0.475)	3874 (0.480)

all states are noninteracting and the calculation of transition properties is gauge-origin independent as long as an appropriate truncation of multipole moment expansions is made.[38–41] An appropriate treatment of electronic relaxation in the core-excited state requires the inclusion of double-electron excitation operators, and we have for that reason adopted the second-order algebraic diagrammatic construction (ADC) polarization propagator method, which has been shown to provide an excellent description of core-excitation processes[21] in the Franck–Condon region. For reference, we will also provide conventional CVS-based time-dependent DFT (TDDFT) calculations of the XAS spectrum of methanol. Standard Kohn–Sham TDDFT is, however, based on a reference state parameterization restricted to single-excitations, and it can therefore not lead to a proper description of relaxation effects. Nevertheless, it is known that CVS-TDDFT calculations of core-electron absorption and emission spectra show a good agreement with experiment once the large self-interaction error inflicted spectral shifts are accounted for.[22]

As an alternative to adopting the CVS approximation, it has been shown possible to address X-ray spectroscopies by means of the complex polarization propagator (CPP) approach,[42–45] which has recently been combined with ADC.[46] By introducing relaxation mechanisms and finite lifetimes of excited states, the CPP approach defines complex response functions in the frequency domain with real and imaginary parts that are related by Kramers–Kronig relations.[42] A frequency region embedded in the spectrum, such as the oxygen K-edge region in the present work, can be addressed without any approximations made in the construction of the propagator (such as the CVS approximation), and this has in turn enabled the derivation and implementation of the *full* electronic polarization propagator for inelastic scattering such as RIXS.[47] We will apply this CPP/ADC method to study the RIXS of methanol, and we note that in regions where the intermediate core-excited states are close in energy, our approach will be particularly advantageous as it encompasses the complete channel interaction between all intermediate states.[28,29]

III. COMPUTATIONAL DETAILS

The geometry optimization and Hessian calculation were performed in C_s symmetry on the level of DFT/B3LYP[31,32] functional and aug-cc-pVTZ basis set[48] in the Gaussian09 software,[49] from which the vibrational frequencies (see Table I) and Wilson coordinate displacements of the normal modes were derived. For comparison, we also determined the equilibrium geometry and normal modes in the CASPT2 framework[19,20] with the ANO-RCC-VTZP[50] basis set (see Table I) and using the MOLCAS program (version 8.2)[51] without imposing symmetry and with 12 electrons in an active space of 12 orbitals. For the calculation of core- and valence-excited states and corresponding transition dipole moments, we used three different methods [restricted active space second-order perturbation theory (RASPT2), CPP-ADC(2), and TDDFT], which are described in detail below.

The computation of ground and core-excited states was performed with the RASSCF method[52] followed by RASPT2.[53] These calculations were scalar relativistic, as implemented in the MOLCAS code (version 8.2)[51] using the Douglas-Kroll-Hess formulation[54,55] and the ANO-RCC-VTZP[50] basis set. The transition dipole moments between the studied electronic states were calculated within the RASSI approach.[34,35] The core-excitation energies and transition dipole moments presented as RASPT2 in Table II were computed at the equilibrium geometry, using an extended Rydberg basis set (8*s*8*p*6*d*) and the C_1 symmetry. Proper treatment of the transition dipole moments is ensured by using the "highly excited-state" (HEXS) approach[56] within the RASSCF method. The three orbitals having atomic orbital characters C1s ($2a'$) and combinations of O2s + C2s ($3a'$) and O2s-C2s ($4a'$) were kept inactive. The O1s ($1a'$) orbital was frozen and placed in a separate part of the active space where its occupancy could be controlled to two for the ground and valence-excited states and to one for core-excited states. The full active space consisted of 13 orbitals, namely, the O1s orbital, five of the occupied orbitals having valence character: $1a''$, $5a'$, $6a'$, $7a'$, $2a''$, and the seven lowest unoccupied orbitals: $8a'$, $9a'$, $3a''$, $10a'$, $11a'$, $12a'$ and $4a''$. The ground state was obtained by a state-specific

TABLE II. Vertical transition energies (eV) (oscillator strengths, f × 10^3) of O(1 s^{-1}) core-excitation from RASPT2, ADC(2)-x, and REW-TDDFT simulations (see Sec. III for details).

	$8\mathscr{A}'$	$9\mathscr{A}'$	$3\mathscr{A}''$	$10\mathscr{A}'$	$11\mathscr{A}'$	$12\mathscr{A}'$
RASPT2	535.04 (9.56)	536.59 (2.83)	537.10 (0.82)	537.11 (1.51)	537.62 (2.36)	537.85 (4.46)
ADC(2)-x	533.05 (8.97)	534.82 (3.23)	535.14 (2.31)	535.15 (1.26)	535.68 (3.35)	535.97 (5.07)
REW-TDDFT	519.34 (7.61)	521.17 (2.86)	521.47 (4.23)	521.56 (1.94)	522.16 (7.82)	522.48 (6.22)
	$4\mathscr{A}''$	$13\mathscr{A}'$	$14\mathscr{A}'$	$5\mathscr{A}''$	$15\mathscr{A}'$	$6\mathscr{A}''$
RASPT2	538.02 (0.11)	...	...	...	...	...
ADC(2)-x	536.13 (0.001)	536.15 (4.71)	536.23 (1.42)	536.25 (0.23)	536.35 (1.91)	536.51 (0.02)
REW-TDDFT	523.08 (3.92)	523.23 (3.81)	523.45 (2.69)	523.46 (0.90)	523.60 (11.63)	524.05 (7.57)
	$7\mathscr{A}''$	$8\mathscr{A}''$	$9\mathscr{A}''$	$10\mathscr{A}''$		
ADC(2)-x	537.31 (0.89)	537.37 (0.69)	537.45 (0.11)	537.62 (0.1)		
REW-TDDFT	524.38 (1.83)	524.39 (5.13)	525.29 (0.56)	526.24 (0.41)		

calculation, while a state-averaging over 7 roots was employed for the core-excited states.

Calculations of core-excitation energies and ground-to-core-excited state transition moments were also performed at the CVS-ADC(2)-x/d-aug-cc-pVTZ level of theory. In addition, complex dipole polarizabilities and RIXS scattering amplitudes were computed at the CPP-ADC(2) approach and the aug-cc-pVTZ basis set. All ADC calculations were performed using a developers version of Q-Chem 5.0.[57]

The PECs of ground and core-excited states were computed along the distortion vectors of 11 normal modes. Because the torsion mode ν_{12} (Table I) has too low frequency (0.036 eV) to be resolved in a RIXS experiment, this mode was excluded from our calculations. The PEC scans were performed with state specific RASPT2 calculations of the ground state (A' symmetry) and the lowest valence excited state of A'' symmetry (to enable studies of electronically inelastic RIXS processes) as described above but with a smaller diffuse Rydberg basis (4*s*4*p*2*d*). The active space was identical to the one described above except that the $4a''$ orbital was removed due to convergence problems. For the core-excited states PECs, we performed a state-averaging over four electronic states for A' symmetry and over two states for A'' symmetry. To increase the computational efficiency while computing the PECs, we constrained the symmetry whenever possible. Hence, for the vibrational modes of A' symmetry, we used the C_s point group, whereas for the A'' symmetry, the C_1 constrain was considered. One should mention that the use or not of symmetry constrains did not significantly affect the energies of the valence- and core-excited states in our simulations.

The TDDFT calculations were performed with the NWChem program[58] using the restricted energy window (REW) approach, which in essence is the same as the CVS approximation. The range-separated CAMB3LYP functional[59] was used with the parameterization proposed in Ref. 43 for core-excitations and in conjunction with Dunning's aug-cc-pVTZ basis set.[48]

Based on the core-transitions calculated with above methods, the XAS and RIXS cross sections [Eq. (9)] were calculated with the use of a modified version of the e*SP*ec program.[26] The numerical solution of the equations presented in Sec. II B was carried out as described in Ref. 26. The main reason for why the proposed scheme is more numerically efficient than carrying out a full $m + n$-dimensional wave packet propagation is related to the intermediate wave packet calculation. Within the discrete variable representation, the number of integrals required to solve Eq. (7) is equal to the total number of points in the grid $N^{(n+m)}$, N being the number of grid points along each dimension. Instead, we only need to solve $k \times N^n$ integrals, where k is the total number of intermediate states included in the m-dimensional Franck-Condon partition. Furthermore, we employ the fast Fourier transform (FFT) to solve Eq. (7). Thus, by taking advantage of the shift theorem, the solution of the integral is reduced to performing N^n FFT evaluations and computing the required 1D Franck-Condon amplitudes.

IV. RESULTS AND DISCUSSION

A. X-ray absorption

Although the XAS spectrum is formed by electron-vibrational transitions, it is instructive to start by presenting the pure electronic core-excitations, which determine the skeleton of the total XAS profile.

1. Electronic contributions to XAS

The XAS was computed using three different quantum chemical tools (RASPT2, ADC(2)-x, and TDDFT) as described in Sec. III. The results of calculations of oscillator strengths f and transition energies are collected in Table II. The corresponding XAS cross sections (Fig. 2), computed with Γ = 0.08 eV and neglecting nuclear motion, display rather strong sensitivity of the XAS profile to the theoretical method. The oscillator strength f is derived from the different quantum chemical approximations, but we plot the XAS

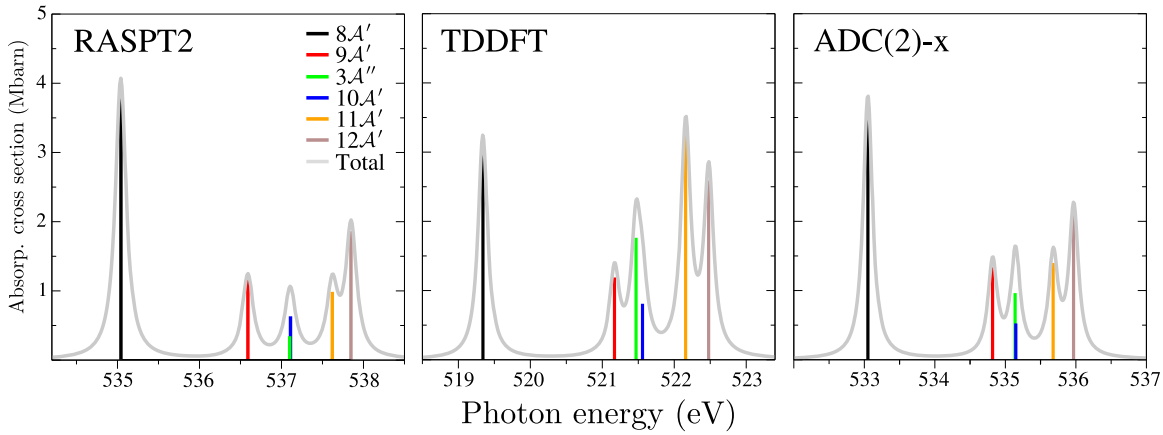

FIG. 2. XAS of gas-phase methanol at the O K-edge, neglecting nuclear motion, with three different methods: RASPT2 (left), TDDFT (middle), and ADC(2)-x (right). Absorption cross sections for each state are shown with the bars of corresponding colors (see legends); the total spectra are obtained by the convolution with the spectral function of half-width at half maximum Γ = 0.08 eV, accounting for the lifetime broadening.

cross sections using the following equation (in SI units) for the cross section at resonance:[60]

$$\sigma_{\mathrm{abs}}(\omega_{\mathrm{res}}) = f\frac{e^2}{2m_e c\varepsilon_0 \Gamma}. \tag{13}$$

We will see below that the theory (Fig. 2) cannot properly reproduce the experiment without taking into account nuclear degrees of freedom. Due to this, we postpone the comparison of the RASPT2, ADC(2)-x, and TDDFT methods with experiment until Sec. IV A 2.

2. Role of nuclear motion in XAS

The methanol molecule has 12 vibrational modes, which are presented in Table I. The mode assignment and experimental frequencies are taken from Ref. 33. To understand the influence of nuclear motion on the XAS, we start with a determination of which normal modes are active. This is done by comparing the PECs of the core-excited states with the ground state PEC, in each state computed along the normal coordinate Q of 11 modes using the RASPT2 method (see Sec. III). Let us remind that the torsion mode ν_{12} is excluded in our simulations because of its too low frequency to influence the spectra. The PECs of the ground and core-excited states of the five active vibrational modes are collected in Fig. 3.

The selected modes are ν_1 (OH-stretching) which is dissociative in the $8\mathcal{A}'$ core-excited state, ν_8 (CO-stretching) which is pseudodissociative in the $8\mathcal{A}'$ and $9\mathcal{A}'$ core-excited states, and ν_7, ν_6, and ν_5 (CH_3-rock, OH-bending, and CH_3 s-deformation,

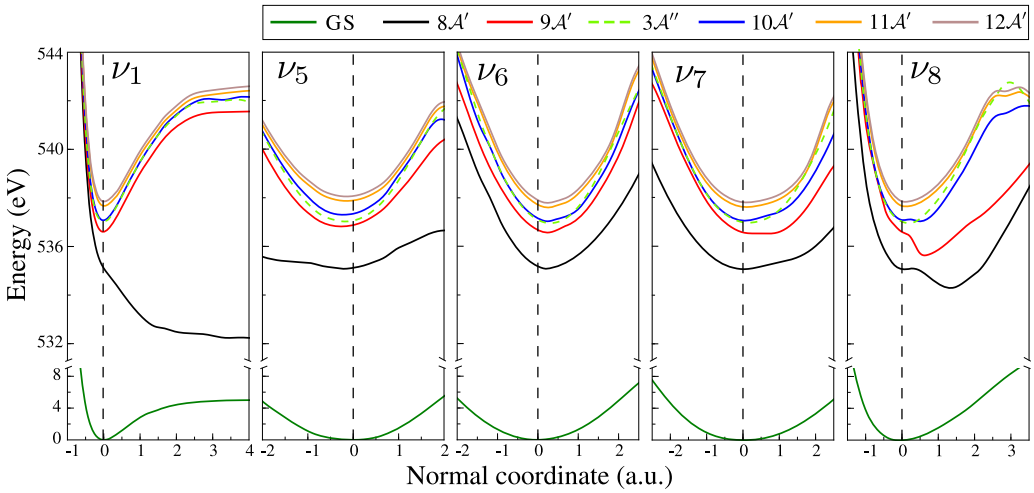

FIG. 3. Potential energy curves along the five most active vibrational modes computed at the RASPT2 level of theory. The ground state (solid green line) and seven lowest core-excited states (see legends for assignment) are shown. Vertical dashed lines show the equilibrium geometry of each mode.

respectively) each of which have a shift of the minimum upon core-excitation. The remaining vibrational modes are not active because the PECs of core excited states are very similar to the PECs of the ground state (see Appendix A and Fig. 15). Furthermore, only a subset of four modes (out of the five modes in Fig. 3) are active for each individual core-excited state,

$$\begin{aligned} 8\mathscr{A}' &: \quad 1\mathrm{D}(\nu_1) + 3\mathrm{D}(\nu_8, \nu_5, \nu_6) \\ 9\mathscr{A}' &: \quad 1\mathrm{D}(\nu_8) + 3\mathrm{D}(\nu_7, \nu_5, \nu_6) \\ 3\mathscr{A}'' &: \quad 1\mathrm{D}(\nu_8) + 3\mathrm{D}(\nu_7, \nu_5, \nu_6) \\ 10\mathscr{A}' &: \quad 1\mathrm{D}(\nu_8) + 3\mathrm{D}(\nu_7, \nu_5, \nu_6) \\ 11\mathscr{A}' &: \quad 1\mathrm{D}(\nu_7) + 3\mathrm{D}(\nu_8, \nu_5, \nu_6) \\ 12\mathscr{A}' &: \quad 1\mathrm{D}(\nu_7) + 3\mathrm{D}(\nu_8, \nu_5, \nu_6). \end{aligned} \tag{14}$$

Here, we order the vibrational modes according to the $1D + 3D$ model outlined in Sec. II B as a general mD + nD representation. Hence, for each core-excitation, the mixed representation treats one mode in the time domain and three modes in the frequency domain. This subselection shown in Eq. (14) was performed as follows. Mode ν_1 was included only for the $8\mathscr{A}'$ state since the PECs are not shifted with respect to the GS for the remaining states (Fig. 3). Mode ν_7 was excluded only for the $8\mathscr{A}'$ state, based on the same shift criterion. To ensure the accuracy of this selection, we carried out 1D calculations of XAS and RIXS for each mode.

The XAS cross section, in which nuclear dynamics is taken into account, is computed in the framework of the $1D + 3D$ model using Eq. (9) and $\Gamma = 0.08$ eV as the lifetime broadening (HWHM) of the O1s core-hole. Here and below, we neglect the dependence of the transition dipole moment on nuclear coordinates, taking $\mathbf{d}_{c0}$ as calculated at the equilibrium geometry. Results of the simulation are depicted in Fig. 4.

A comparison of the computed XAS profiles without (Fig. 2) and with nuclear dynamics (Fig. 4) shows the importance of nuclear motion for an accurate description of the XAS. This is because the PECs are different for distinct core-excited states. To demonstrate clearly the effect of nuclear degrees of freedom on the XAS profile, we present an additional spectrum, in which the same transition dipole moment was deliberately used for all core-excited states (see Fig. 4). The main effect is seen already in the strong broadening and intensity reduction of the first ($8\mathscr{A}'$) XAS peak. The reason for this is that PEC of ν_1 mode becomes repulsive under core-excitation, similar to gas phase and liquid water,[4,6] where the molecule dissociates into a hydrogen atom and a core-excited methoxy radical $CH_3O^*\cdot$. We see that the agreement with experiment[17] improves for all theoretical methods when the nuclear motion is taken into account. One should notice that the ADC(2)-x and RASPT2 methods give better agreement with the experiment[17] from the point of view of both intensity distribution and the peak positions (Fig. 4). Let us note that here we compare the transition dipole moments and

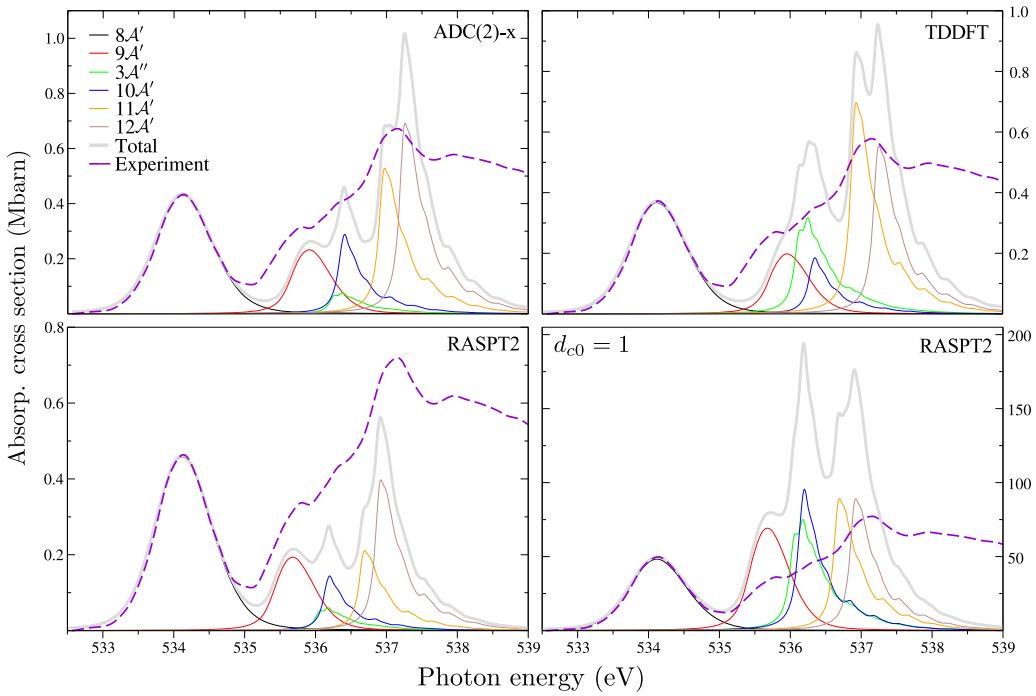

FIG. 4. XAS spectrum of the gas phase of methanol at the O K edge taking into account nuclear motion compared to experiment.[17] To focus on the intensity distribution of XAS, the theoretical profiles are shifted to match the first experimental peak $8\mathscr{A}'$. The actual transition energy of the first peak for each theoretical method is given in Table II. The lower right panel shows a hypothetical absorption spectrum where the electronic transition dipole moments are set to one, to isolate the purely vibrational contributions.

core-excitation energies from different methods, whereas the PEC shapes are taken from the RASPT2 calculations in all cases, as described in Sec. III.

B. Quasi-elastic resonant X-ray scattering: Nuclear dynamics

In this section, we consider the RIXS which ends up in the electronic ground state and focus on the two lowest core excited states $8\mathscr{A}'$ (Fig. 5) and $9\mathscr{A}'$ (Fig. 6). As one can see from the PECs (Fig. 3), methanol dissociates along the OH bond in the first core-excited state, $8\mathscr{A}'$, while all modes have bound PECs for the second core-excited state, $9\mathscr{A}'$. This is the main reason for such a strong difference in the vibrational progression of $8\mathscr{A}'$ and $9\mathscr{A}'$ RIXS channels. The RIXS spectra are simulated in the framework of the 1D + 3D model as it was outlined in Sec. II B, just as the XAS spectra presented above. Again, we use the BO approximation and assume that the vibrational modes are uncoupled. We employed the same active vibrational modes as selected for the simulation of XAS [Eq. (14)] because only the ground and core-excited states participate in the quasi-elastic RIXS process.

1. The RIXS via the dissociative $8\mathscr{A}'$ core-excited state

When the photon energy is tuned in resonance with the $8\mathscr{A}'$ state, the methanol molecule dissociates along the OH bond (Fig. 3).

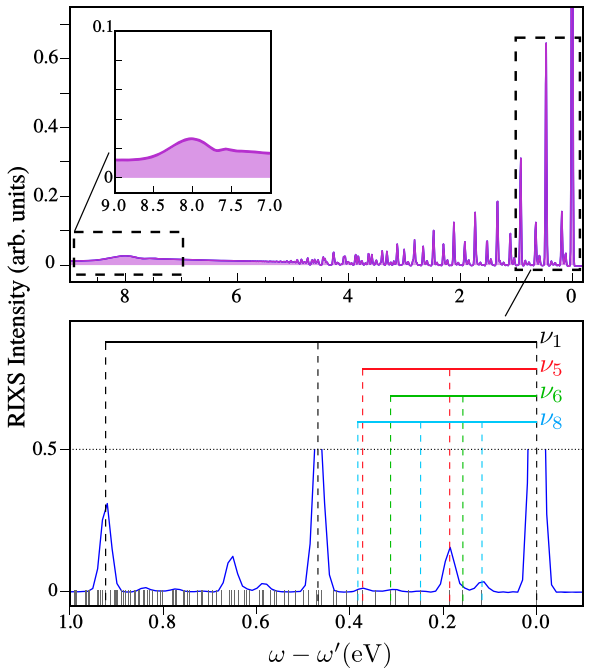

FIG. 5. Profile of quasi-elastic RIXS. Photon energy is tuned in resonance with the dissociative $|1a'^{-1}8a'^{1}\rangle$ core-excited state. The lower panel shows a zoom of the RIXS spectrum in the region [−0.1 to 1.0 eV] with assignment of the main vibrational progressions of the ν_1, ν_5, ν_6, and ν_8 modes. The black bars illustrate all possible vibrational overtones of these modes.

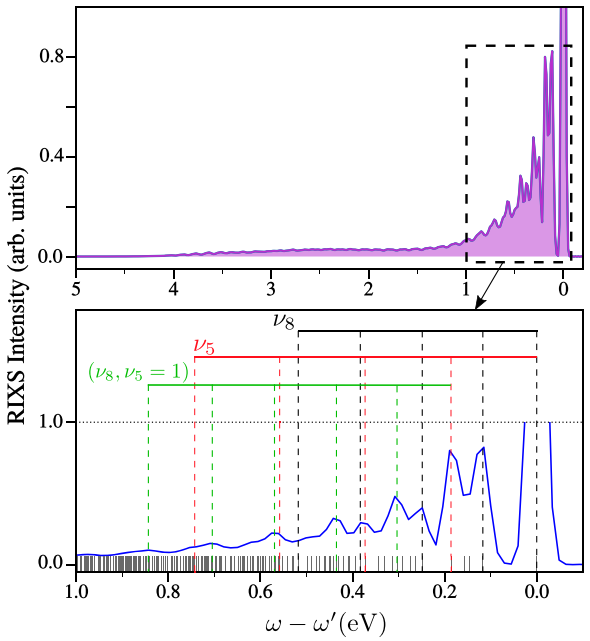

FIG. 6. Profile of quasi-elastic RIXS. Photon energy is tuned in resonance with bound $|1a'^{-1}9a'^{1}\rangle$ core-excited state. The lower panel shows a zoom of the RIXS spectrum in the region [−0.1 to 1.0 eV] with the assignment of the two main vibrational progressions of the ν_8 and ν_5 modes, as well as an overtone progression (ν_8, ν_5 = 1) given its significant contribution to the spectrum. The black bars illustrate all possible vibrational overtones of the four modes ν_5, ν_6, ν_7, and ν_8 taken into account.

The small mass of hydrogen means that the nuclear wave packet can move far away from equilibrium along the OH bond during the core-hole lifetime in the dissociative PEC of the $8\mathscr{A}'$ state. This results in the population of high ν_1 vibrational levels upon decay to the ground state and explains the origin of the extensive progression in RIXS for the OH stretching mode (Fig. 5). This progression forms the so-called molecular band[27,28] with its maximum at $\omega - \omega' = 0$. The other vibrational modes remain bound under core-excitation, and hence, their vibrational progressions are much shorter. Therefore, the role of the remaining vibrational modes is only "to dress" the OH skeleton in overtones, as seen in the lower panel of Fig. 5. We characterize the vibrational resonances in RIXS by $n = (\nu_1, \nu_8, \nu_6, \nu_5)$ composed of the active modes in this channel [see Eq. (14)].

Due to ultrafast dissociation along the OH bond, with kinetic energy release of about 3 eV, the nuclear wave packet has time to reach the region of dissociation during the lifetime of the core-excited state. The decay transition in the fragment of dissociation, the core-excited methoxy radical ($CH_3O^*\cdot$), results in the appearance of a peak at $\omega - \omega' \approx 8$ eV, which we denote as the *atomic-like peak*, following the well-established terminology used for ultrafast dissociation in diatomic molecules.[27,28,61] Note that the width of the atomic-like peak is significantly larger than the natural broadening (HWHM) $\Gamma = 0.08$ eV (Fig. 5). The reason for this is the vibrational structure of the methoxy radical.

It is crucial to mention that the atomic-like peak, described here, lies in the same energy region as electronically inelastic features and hence is not observable as an isolated peak. Nevertheless, a closely related feature, which we refer to as a *pseudo-atomic peak*,[62] is formed in the decay to the lowest valence excited state. However, in sharp contrast to the atomic-like peak, it is formed close to the equilibrium geometry. We will discuss the intricacies of the atomic-like and pseudo-atomic peaks in detail in Sec. IV C.

2. Control of the nuclear dynamics via the variable scattering duration

As it is well known, the RIXS profile is very sensitive to the scattering duration[28,63]

$$\tau = \frac{1}{\sqrt{\Omega^2 + \Gamma^2}}, \tag{15}$$

which is controlled by detuning from the top of the XAS resonance $\Omega = \omega - \omega_{\text{top}}$. To make the picture complete, it is instructive to explore the Ω dependence of the RIXS spectra around the $8\mathscr{A}'$ absorption resonance, as shown in Fig. 7.

One can see, as we tune below the top of absorption, that the atomic-like peak gradually vanishes (Fig. 7). The intensity of this peak drops down sufficiently already at $\Omega = -0.5$ eV, and it disappears completely already at $\Omega = -0.75$ eV. Simultaneously to the quenching of the atomic-like peak, one can see the shortening of the vibrational progression with an increase in $|\Omega|$. Both these observations are due to the shortening of the scattering duration so that the wave packet propagates only a short distance away from the equilibrium geometry. Finally, the whole RIXS profile collapses to the Rayleigh line[64,65] at $\Omega < -1.5$ eV.

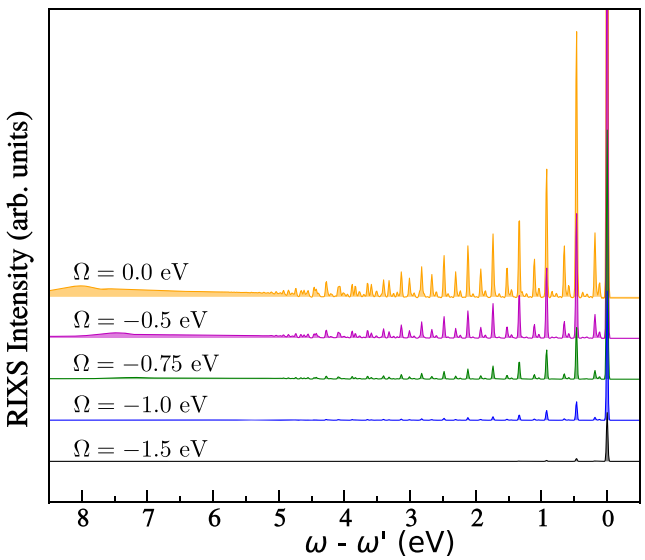

FIG. 7. Dependence of the RIXS profile on the detuning Ω near the first core-excited state $|1a'^{-1}8a'^{1}\rangle$, which illustrates the collapse of the vibrational progression at large values of Ω due to the decrease in the effective scattering duration time τ; see (15).

Another effect related to energy detuning is the purification of the RIXS spectra when $|\Omega|$ increases. As observed from Fig. 7, the intensity of the overtones related to the soft modes (Fig. 5) decreases faster than that related to the high frequency OH stretching mode.[66] Already at $\Omega = -0.75$ eV, one can barely see overtones and only the main ν_1 vibrational progression remains. This is because the other modes have no time to perform an oscillation when the period is longer than the scattering duration

$$\tau < T_{vib} = \frac{2\pi}{\omega_{vib}}. \tag{16}$$

3. The RIXS via the bound $9\mathscr{A}'$ core-excited state

Let us turn our attention to the RIXS through the second core-excited state $9\mathscr{A}'$ shown in Fig. 6. Here, we assigned vibrational resonances of ground state by $n = (\nu_8, \nu_7, \nu_6, \nu_5)$ according to Eq. (14). Contrary to RIXS through $8\mathscr{A}'$ (Fig. 5), the OH stretching mode is not active in this channel. Therefore, we see a significant shortening of the vibrational progression which is confined in the region $0 \le \omega - \omega' \lesssim 1$ eV. This is because the core-excited wave packet does not propagate far from the equilibrium due to the bound nature of the PECs. The core-excited dynamics at the $9\mathscr{A}'$ state is mostly affected by the ν_8 and ν_5 normal modes, as it is seen in Fig. 6. The second and third peaks, in the RIXS spectrum, are predominantly formed from the first excited vibrational states of the ν_8 and ν_5 modes, respectively, with smaller contributions from the ν_6 and ν_7 modes. The total vibrational progression is made up of $(\nu_8, 0, 0, 0)$ and $(0, 0, 0, \nu_5)$, and both are dressed by mixed excitations, or overtones. At energy loss $\omega - \omega' > 0.5$ eV, we observe the formation of a "tail" due to the high density of close-lying vibrational levels corresponding to mixed overtones of different modes.

C. Dynamical origin of the splitting of the $2a''$ peak

Let us come back to the RIXS via core-excitation to state $8\mathscr{A}'$, where methanol dissociates along the normal coordinate $Q \equiv Q_{\nu_1}$ which corresponds to elongation of the OH bond. In Sec. IV B 1, the atomic-like feature[27,28,61,67] at $\omega - \omega' \approx 8$ eV (Fig. 5) was discussed and attributed solely to the transition to the ground state of the product of the dissociation, core-excited methoxy radical CH_3O^*.

$$\omega + \mathrm{CH_3OH} \rightarrow \mathrm{CH_3O^*\cdot} \rightarrow \mathrm{CH_3O\cdot + H} + \omega'. \tag{17}$$

However, as briefly mentioned at the end of Sec. IV B 1, there is another RIXS channel which also contributes to the features lying in this energy region. This is expected since the methoxy radical belongs to the C_{3v} point group with a doubly degenerate X^2E ground state.[68] Hence, two electronic states of methanol should have the same dissociation limit along the OH stretch, namely, the ground state $|GS\rangle = |1A'\rangle$ and the dissociative $|2a''^{-1}8a'^{1}\rangle$ state (see Fig. 8). Therefore, we need to account for two overlapping RIXS features: The first one studied in Sec. IV B ends up in the ground state $|GS\rangle$, while the final dissociative valence excited state $|2a''^{-1}8a'^{1}\rangle$ gives rise to the second RIXS channel. Let us now investigate the gross features of these channels, namely, the molecular band and the atomic-like peak. For this purpose, we employ a 1D model,

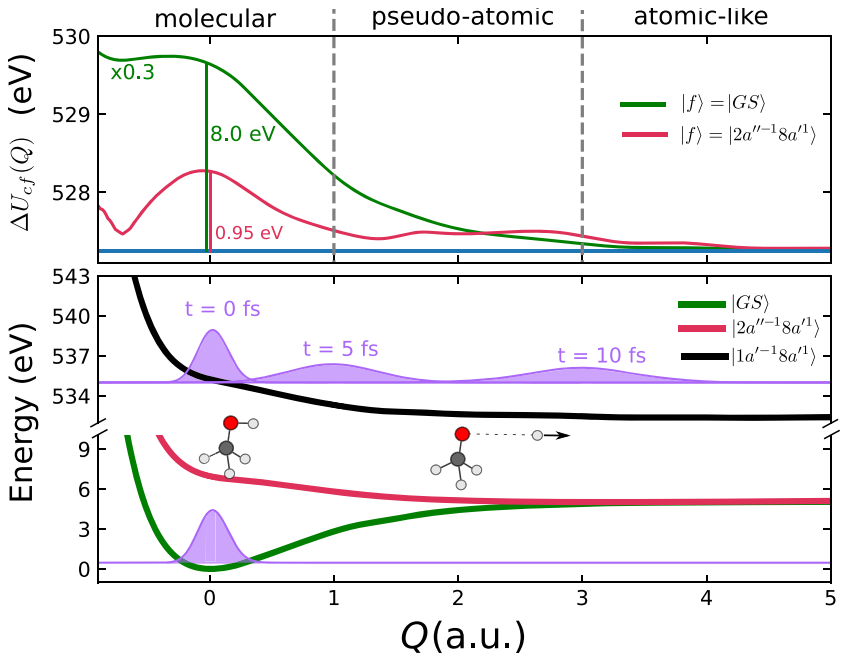

FIG. 8. Potential energy curves for the ground, core-excited $8\mathscr{A}'$, and final dissociative $|2a''^{-1}8a'^{1}\rangle$ states together with the evolution in core excited state of square of nuclear wave packet, $|\psi_c(t)|^2$ (lower plot). The lifetime decay of $\psi_c(t)$ accounted by factor $e^{-\Gamma t}$ in Eq. (7) is not shown here. Functions $\Delta U_{cf}(Q) = U_c(Q) - U_f(Q)$ (lower plot) for the ground (green line) and the first valence excited (red line) states show the transition emission energy at distance Q. Approximately divided regions of formation of the molecular band, pseudo-atomic, and atomic-like peaks are labeled on the top of the upper plot.

taking into account only the ν_1 mode, which is the most active coordinate.

The computed total RIXS spectra and the partial contributions from each channel are shown in the upper and lower panels of Fig. 9, respectively, for both CH_3OH and CH_3OD. The quantitative details of the observed dependences on the photon polarization and isotopic substitution will be discussed below; for now, we shall focus on understanding the contributions of different channels to the total

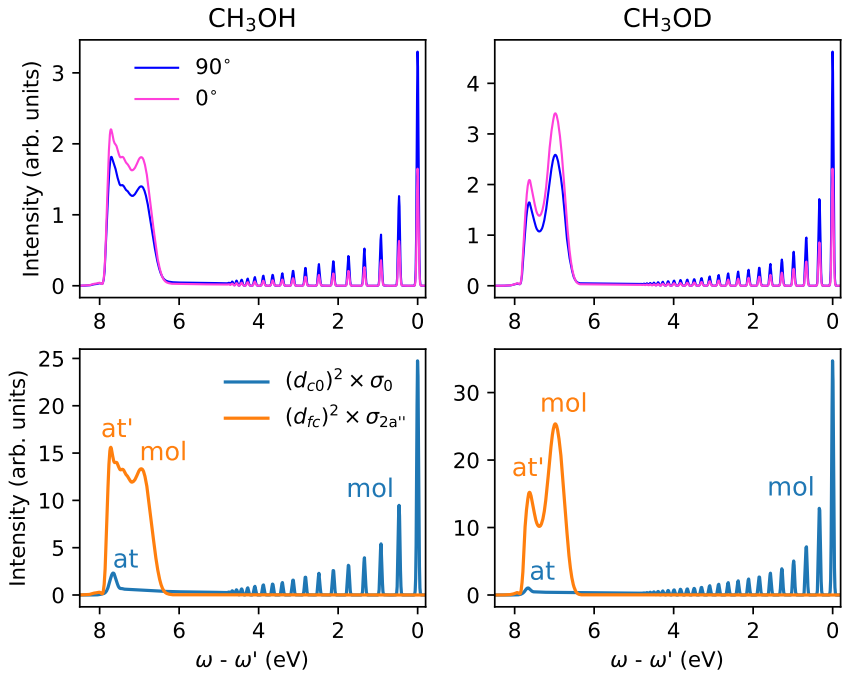

FIG. 9. RIXS via the lowest core-excited state $|1a'^{-1}8a'^{1}\rangle$ for CH_3OH (left panels) and CH_3OD (right panels). Upper panels display the polarization dependence of the RIXS cross sections, where $\chi = \angle(\mathbf{e}, \mathbf{k}') = 0°$ and 90° (see legend). The lower panels show the partial contributions to the RIXS cross section (18) from the scattering channels to the ground state (blue line) and to the lowest valence excited state $|2a''^{-1}8a'^{1}\rangle$ (orange line). Contribution of the atomic-like (at), pseudo-atomic (at′), and molecular (mol) bands is labeled for both channels. The spacing between the pseudo-atomic peak (at′) and maximum of the molecular band (mol) is equal to 7.71 eV and 0.76 eV, respectively, for the RIXS channel which ends up in the ground state and in the $|2a''^{-1}8a'^{1}\rangle$ valence excited state.

profile. Evidently, both RIXS channels contribute to the atomic-like peak formed in the dissociation region since the ground and valence-excited states have the same dissociative limit (Fig. 8). However, the contribution of the valence channel to this spectral region also involves decay transitions near the equilibrium geometry since the potentials of the core- and valence-excited states become parallel already around $Q \approx 1.0$ a.u. Thereby, a pseudo-atomic peak (marked as "*at*'" in Fig. 9) is formed. The pseudo-atomic peak has the same transition energy but much higher intensity than a real atomic-like peak (marked as "*at*" in Fig. 9). The reason for this is that only a small fraction of the nuclear wave packet reaches the dissociation region ($Q \geq 3.0$ a.u.) in the core-exited state due to the short lifetime on the core-excited states (Fig. 8). Let us discuss this non-trivial formation of RIXS to the valence excited state in more detail.

The RIXS profile depends on the PECs of the core-excited and final states. This motivates us to look on the difference of the PECs $\Delta U_{cf}(Q) = U_c(Q) - U_f(Q)$ for final states $|f\rangle = |GS\rangle$ and $|f\rangle = |2a''^{-1}8a'^{1}\rangle$ (Fig. 8). It is well known that the molecular band and the atomic peak, in diatomics, strictly coincide with each other when the PECs of core-excited and final states are exactly parallel.[28] One can see (Fig. 8) that the PEC of the final $|2a''^{-1}8a'^{1}\rangle$ state is almost parallel to the one of the core-excited states, contrary to the ground final state. Figure 8 shows that the region of formation of the pseudo-atomic peak, defined by the condition $\Delta U_{cf}(Q) = \text{const}$, starts at $Q \approx 1$ a.u. for the valence final state $|2a''^{-1}8a'^{1}\rangle$, while for the ground final state, the formation of the atomic-like peak starts for longer distances $Q \gtrsim 3$ a.u. It takes about 5 fs for the wave packet to reach $Q \approx 1$ a.u. and 10 fs for $Q \approx 3$ a.u. For the RIXS channel to the ground state, the maxima of the atomic-like peak and the molecular band are separated by $\omega'_{\text{mol}} - \omega'_{\text{at}} \approx \Delta U_{c0}(0) - U_{c0}(\infty) = 8$ eV (Fig. 8). By contrast, the scattering to the dissociative $|2a''^{-1}8a'^{1}\rangle$ state is expected to have close lying pseudo-atomic and molecular peaks with the spacing of only $\omega'_{\text{mol}} - \omega'_{\text{at}} \approx \Delta U_{cf}(0) - U_{cf}(1\text{ a.u.}) = 0.95$ eV (Fig. 8). This expectation is nicely confirmed by the simulated RIXS profile (Fig. 10) with $\omega'_{\text{mol}} - \omega'_{\text{at}} = 0.76$ eV. We notice that a similar behavior has been observed in the water molecule.[62] In summary, despite the fact that they occur at nearly the same emission energy, the nature of the pseudo-atomic and atomic-like peaks arising in the RIXS to the valence-excited and ground states, respectively, is different. The decay in the core-excited fragment of dissociation, the methoxy radical, forms an atomic-like peak when the final state is the ground electronic state. Contrary to the ground state RIXS channel, the origin of the pseudo-atomic peak for the $|2a''^{-1}8a'^{1}\rangle$ RIXS channel is mainly the decay transition in CH_3OH not far from the equilibrium geometry and its energy position is rather close to the molecular band (Figs. 8 and 10). Despite their inherent differences, they are both dynamical features that behave analogously with respect to isotopic substitution and excitation energy detuning, as we describe below.

Results of the 1D simulations of the RIXS profile, shown in Fig. 10, demonstrate the role of isotopic substitution. First of all, one can see the effect of the isotopic substitution on the vibrational progression, originated from decay to the ground-state. The observed difference is simply caused by the difference in OH and OD vibrational frequencies. The second effect we observe is mainly due to the pseudo-atomic peak, formed upon decay to the $2a''$ state, and is related to the slowdown of the nuclear wave packet in the dissociative core-excited state of CH_3OD in comparison with CH_3OH, because of the heavier deuterium atom. This makes the pseudo-atomic peak in RIXS of CH_3OD less intense than in the CH_3OH, which is in good agreement with the experiment[18] (Fig. 10).

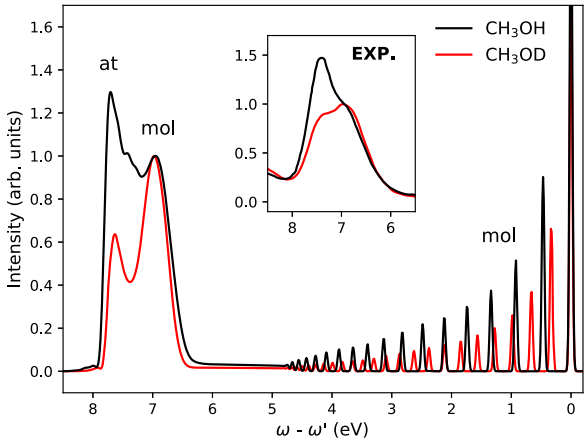

FIG. 10. Role of the isotopic substitution: MeOH vs MeOD. For both molecules, the atomic feature (at) of the total profile (including both RIXS channels ending up in the ground state and in the $|2a''^{-1}8a'^{1}\rangle$ valence excited state, respectively) consists of atomic-like and pseudo-atomic contributions (see Fig. 9). $\chi = 90°$. The inset shows the corresponding experimental spectra taken from Ref. 18.

There is also another tool to distinguish pseudo-atomic and molecular peaks: The dispersion law. As it is well known,[27,28] the emission energy of the pseudo-atomic peak should not depend on the excitation energy ω, as opposed to the molecular band which has Raman dispersion (see Fig. 11). One should notice that the role of the ground state RIXS channel in formation of the pseudo-atomic peak near $\omega - \omega' \approx 8$ eV is rather weak in contrast to the region of vibrational progression $0 \leq \omega - \omega' \lesssim 5$ eV (see lower panel in Fig. 9). Similarly to the quasi-elastic channel, shown in Fig. 7, the intensity of the pseudo-atomic peak formed in the inelastic channel (Fig. 11) drops as we tune away from the top of the $8\mathscr{A}'$ XAS resonance. To conclude, one should stress that the RIXS channel to the $|2a''^{-1}8a'^{1}\rangle$ final state would have only a molecular peak if the nuclear motion were neglected. However, the dissociation of the core excited methanol molecule along the ν_1 PEC of this state results in an additional resonance, the pseudo-atomic peak. Thus, the splitting of the $|2a''^{-1}8a'^{1}\rangle$ resonance is dynamical in nature.

Finally, let us turn our attention to the polarization dependence of the studied RIXS profile which can be significant due to different orientations of the decay transition dipole moments $\mathbf{d}_{c0}$ and $\mathbf{d}_{2a''}$ to the ground and to the $|2a''^{-1}8a'^{1}\rangle$ states, respectively. Indeed, the transition dipole moments $\mathbf{d}_{c0}$ and $\mathbf{d}_{2a''}$ of these channels are orthogonal to each other (see Table III) since the molecular orbital $8a'$ is lying in the molecular plane, while the $2a''$ orbital is orthogonal to this plane because of its π character (Fig. 1). Due to this and Eqs. (10)

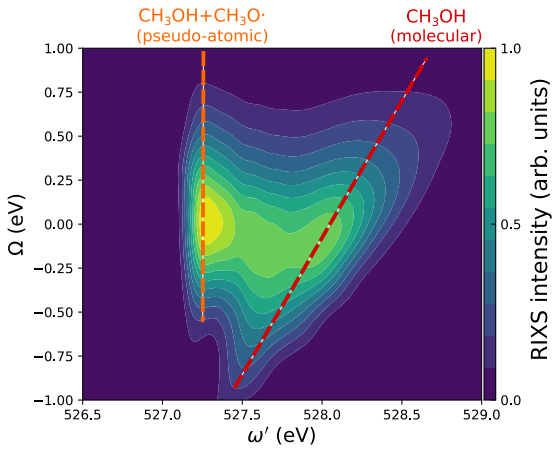

FIG. 11. RIXS map of the $|2a''^{-1}8a'^{1}\rangle$ peak: the vertical axis shows excitation energy as detuning $\Omega = \omega - \omega_{top}$ from the top of the lowest core-excited resonance $|1a'^{-1}8a'^{1}\rangle$, and the horizontal axis corresponds to the RIXS emission energy. The position of the pseudo-atomic peak (decay both in CH_3OH and $CH_3O\cdot$) does not depend on the excitation energy ω. By contrast, the molecular band (decay in CH_3OH) is dispersive.

and (11), the total RIXS cross section in Eq. (9) in the region $\omega - \omega' \lesssim 8$ eV is the sum of two contributions with different polarization dependences,

$$\sigma(\omega', \omega) = \frac{d_{c0}^2}{30}\left[d_{c0}^2 2(2 - \cos^2\chi)\sigma_0 + d_{2a''}^2(3 + \cos^2\chi)\sigma_{2a''}\right]. \quad (18)$$

The partial cross sections σ_0 and $\sigma_{2a''}$ corresponding to the RIXS to the ground and $|2a''^{-1}8a'^{1}\rangle$ states, respectively are computed using Eq. (9) with $D_{c0} = D_{fc} = 1$ within one-dimensional model (Fig. 8) taking into account only elongation of the OH bond. As expected, the RIXS profile in Eq. (18), shown in Fig. 9, displays a strong scattering anisotropy for both CH_3OH and CH_3OD.

D. Inelastic X-ray Raman scattering (electronic degrees of freedom)

Response calculations for RIXS transition strengths were performed using the CPP-ADC approach. In this work, we limited ourselves to the second-order ADC(2) model for the response calculation. However, we point out that by using higher order models, the description of the valence-excited states can be improved as we discuss in a more detailed analysis found in Appendix B. The calculation of RIXS spectra was limited to setting frequencies of the incident field equal to the transition frequencies of the first two absorption peaks in the corresponding XAS spectrum, i.e., 534.29 and 535.46 eV for transitions $a' \rightarrow 8a'$ and $a' \rightarrow 9a'$, respectively. The RIXS scattering amplitude matrices were computed for each frequency taking the first 35 valence-excited states in each irreducible representation into account. Based on the scattering amplitudes, RIXS transition strengths were evaluated for different angles (0°, 45°, and 90°) between the wave vector of the incident radiation and the propagation vector of the outgoing photon. For the comparison of our simulated spectra with the experimental spectra of Benkert,[18] we will start by briefly restating the key elements of our theoretical approach and the experimental assignment.

In our CPP-ADC(2) approach, we evaluate the contribution to the RIXS transition strength for each individual final valence-excited state. This results in the stick spectra given in Fig. 12, where the peak heights are defined by the RIXS transition strength for the different angles and the peak positions are defined by the energy loss, i.e., the energy of the incident photons less than the respective valence-excitation energy. By including the 35 lowest states in each irreducible representation, we recover all valence-excited states with an excitation energy smaller than 15.5 eV, or, in other words, an emission photon energy of 520 eV. On the technical side, we point out that we chose the aug-cc-pVTZ basis set for this part of our study to avoid artificial valence–Rydberg mixing in the description of the final states in the scattering process. Including more diffuse functions would lead to an artificially higher density of states in the chosen spectral window of 0–15.5 eV. The valence eigenstates are calculated without a lifetime and vibrational broadening in contrast to the intrinsically included lifetime broadening of the core-excited states. Thus, in order to obtain spectra comparable with the experimental ones, a summation of Lorentzian-broadened (broadening of 0.25 eV) contributions to the RIXS transition strength of each valence-excited final state has been carried out.

The assignment of the spectral features performed by the experimentalists is based on a single-particle picture. In this picture, the core-excited state is described by a vacant core orbital (core-hole) and an electron occupying a virtual orbital. Each peak is labeled with a decay transition to the respective core-hole from different occupied orbitals, yielding the final valence-excited state. To 0-th order, these states can be described by single-reference configurations based on the Hartree–Fock orbitals. However, our second-order ADC approach describes both the core- and valence-excited states as correlated states, i.e., as multireference configurations. Still, the states are dominated by the 0-th order contribution, which justifies labeling the states by the largest entry in the excitation vector.

TABLE III. Components of the transition dipole moments (in a.u.) from RASPT2 calculations in the frame shown in Fig. 1.

Transition	d_x	d_y	d_z	$d = \lvert\mathbf{d}\rvert$
GS→ $\lvert 1s_O^{-1}8a'^{1}\rangle$	−0.008 17	−0.030 40	0.000 00	$d_{c0} = 0.031\,48$
$\lvert 1s_O^{-1}8a'^{1}\rangle \rightarrow \lvert 2a''^{-1}8a'^{1}\rangle$	0.000 00	0.000 00	−0.055 19	$d_{2a''} = 0.055\,19$

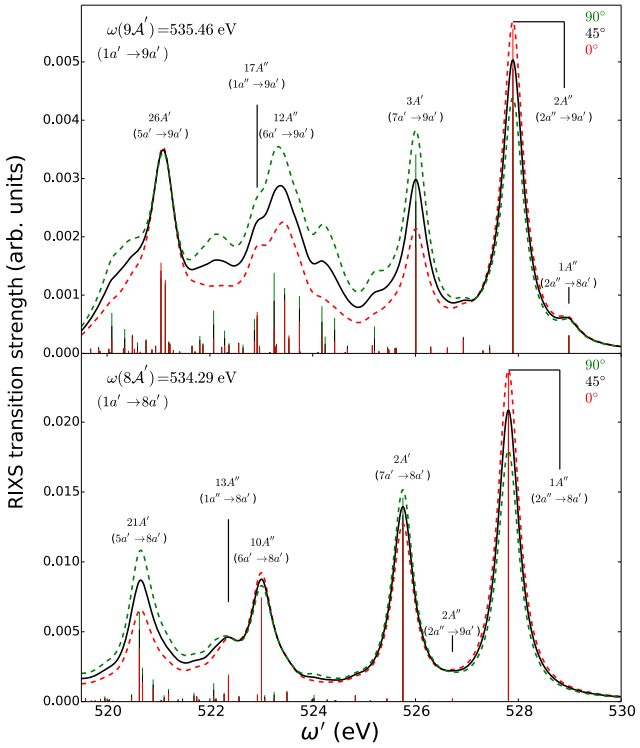

FIG. 12. RIXS spectra of methanol via the two lowest core-excited states $|1a'^{-1}8a'^{1}\rangle$ (lower panel) and $|1a'^{-1}9a'^{1}\rangle$ (upper panel) simulated at the CPP-ADC(2)/aug-cc-pVTZ level of theory. Angular dependence is shown for χ = 0°, 45°, and 90° with red, black, and green curves, respectively. The sticks represent the contribution of individual final states to the RIXS transition strength; the assignment of the main contributions based on one electron transitions is given next to each peak. The curves have been obtained by summing up Lorentzian-broadened (broadening 0.25 eV) contributions.

This labeling makes it possible to compare our simulated spectra to the experimental ones. It should be noted that in the case of ADC, the entries of the excitation vector refer to the dynamically correlated basis of the so-called intermediate state representation (ISR), which, again to 0-th order, can be viewed as single-reference states.

The spectra in Fig. 12, resulting at the resonance frequency of the first core-excited state, show five main peaks. The peak-labels for the spectrum of the $8\mathscr{A}'$ state refer to the valence-excited state with the largest RIXS transition strength under the respective peak. In addition, the largest entry in the excitation vector is given for each state. The assignment based on the excitation vectors is in agreement with that previously derived by the experimentalists. For the spectra of the second core-excited state, the transitions corresponding to the same valence-occupied orbitals are shifted to higher energies, again agreeing with experiment.

To discuss the details of the simulated spectra, we look at the contributions from the two lowest valence-excited states $1A''$ and $2A''$. The largest peak in the lower panel of Fig. 12 originates from the $1A''$ state and corresponds to a relaxation of the first core-excited state $8\mathscr{A}'$ in terms of filling the $1a'$ core-hole with an electron from the $2a''$ valence orbital. Less intuitively, the same valence state also gives rise to a peak in the RIXS spectrum in resonance with the second core-excited state $9\mathscr{A}'$; in this case, it appears as a shoulder, which is blue-shifted with respect to the $2A''$ peak. This shoulder peak has two qualitatively different contributions of comparable sizes. The first contribution is due to the multireference nature of the involved states. As a result, the valence $1A''$ state is coupled to the second core-excited state and shows a nonzero transition-dipole moment despite the fact that the 0th order wave functions differ in occupation by a two-electron excitation. The second contribution, which is even more important in this case and gives rise to the majority of the intensity of the $1A''$ in the upper part of Fig. 12, is due to nonresonant inelastic scattering. The nonresonant contribution at the frequency of the $9\mathscr{A}'$ state originates, for example, from weak nonresonant population of the $8\mathscr{A}'$ core-excited state followed by strong decay to the $1A''$ final state. The nonresonant scattering channel contributes to the real components of the scattering amplitude matrix, which are larger than the imaginary resonant contributions at the same frequency for the $1A''$ state. Likewise, for the $2A''$ state, it appears as a strong peak in the spectrum at the frequency in resonance with the $9\mathscr{A}'$ state but only as a weak spectral feature at the frequency in resonance with the $8\mathscr{A}'$ state. We emphasize that a quantitative description of this nonresonant inelastic scattering effect is only achieved by including the full summation in the Kramers-Heisenberg expression.[28]

Overall, a large number of valence-excited states contribute to the spectral shape. This leads to additional features, especially for the second core-excited state in the region between the peaks of the $7a' \rightarrow 9a'$ and $5a' \rightarrow 9a'$ transitions. Here, the additional peaks besides those originating from the $1a''$ and the $6a'$ orbitals stem from transition with significant Rydberg-character. The higher density of states in the high valence-energy region (lower emission photon energy) can be understood as a consequence of a growing number of possible configurations in the mixing of the states involving higher-lying unoccupied orbitals with increasingly diffuse character.

The first RIXS transition $2a'' \rightarrow 1s_O$ deserves a special comment. Contrary to transitions from other MOs, the peak position of this resonance is almost insensitive to the intermediate core-excited state. Indeed, the spacing between the RIXS peaks for final states $2a'' \rightarrow 8a'$ and $2a'' \rightarrow 9a'$ is very small, 0.088 eV (see Fig. 12). The reason for this is the nonbonding character of the $2a''$ orbital which behaves rather similarly to the $1s_O$ orbital (like the $1b_1$ orbital in H_2O molecule[47]). This makes the $2a'' \rightarrow 1s_O$ transition very special in RIXS of liquid methanol (see Sec. IV E) and similar to the $1b_1 \rightarrow 1s_O$ transition in liquid water.[4,6,69]

Finally, we look at the angular dependence of the RIXS profile in Fig. 12. To understand this dependence, one should look at Eq. (11), assuming for simplicity that $(\hat{\mathbf{d}}_{\mathscr{A}'} \cdot \hat{\mathbf{d}}_{A'})^2 = 1$,

$$\sigma_{\mathscr{A}'A''} \propto 3 + \cos^2\chi, \quad \sigma_{\mathscr{A}'A'} \propto 2 - \cos^2\chi. \tag{19}$$

Here, the first channel $\sigma_{\mathscr{A}'A''}$ corresponds to the peaks $2a'' \rightarrow 8a'$ and $2a'' \rightarrow 9a'$, while the peaks $7a' \rightarrow 8a'$ and $7a' \rightarrow 9a'$ are described by the cross section $\sigma_{\mathscr{A}'A'}$ in Fig. 12. In agreement with Eq. (19), the

RIXS peaks $2a'' \rightarrow na'$ and $7a' \rightarrow na'$ display opposite dependence on the angle $\chi = \angle(\mathbf{e}, \mathbf{k}')$.

E. Aspects of RIXS from liquid methanol

The understanding of the formation of the RIXS spectrum of gas phase methanol provides a robust foundation to shed light on RIXS of methanol in the liquid phase. The quasi-elastic RIXS differs qualitatively from electronically inelastic resonant X-ray scattering. This type of RIXS shows a nicely resolved vibrational structure in different aggregate states of matter: crystalline and amorphous solids,[70] liquid acetone,[66] and water.[2,4,71] RIXS experiments have been performed at the ADRESS—X03MA beamline[72] at the Swiss Light Source, Paul Scherrer Institut, Villigen, Switzerland, using the SAXES spectrometer[73] with a combined spectral resolution of 50–60 meV in our measurements. Liquid samples were prepared in a flow-cell with a 150 nm thick Si_3N_4 window coated with 10 nm gold on the inside. The sample in the interaction region was renewed during the measurements. Linearly polarized X-rays were used with the polarization vector perpendicular to the scattering plane defined by the incident x-ray beam and the direction of detection. The energy calibration was based on the vibrationally resolved O_2 spectrum.[74] These new measurements with much better resolution in comparison with the earlier experiment[15] nicely resolve vibrational structure of RIXS as it is shown in Fig. 13 for the photon energy tuned in the resonance with the pre-edge peak of the OK XAS. The raw experimental RIXS spectrum contained two symmetric artifacts due to X-ray optics at approximately ±0.65 eV with respect to the elastic line. This artifact, presented as an isolated peak on the red side of the spectrum, was mirror reflected to the blue part of the spectrum and subtracted from the raw data to generate the artifact-free spectrum shown in Fig. 13.

Although our simulations are performed for free methanol molecules, the comparison of the simulations with the experiment for liquid methanol shows that the gas phase quasi-elastic RIXS is rather similar to the RIXS of the liquid phase. The experimental quasi-elastic RIXS of liquid methanol displays the OH vibrational progression with a vibrational frequency of $\omega_{\nu_1} = 0.425$ eV which is rather close to the experimental IR frequency $\omega_{\nu_1} = 0.456$ eV (see Table I). One can see that the vibrational progression in the liquid phase is significantly shorter than in gas phase methanol. The reason for this is the strong fluctuation of the outermost part of the OH potential due to fluctuation of the hydrogen bond network. This results in a randomization of the high energy part of the RIXS spectrum of liquid methanol similar to the RIXS of liquid water[4] and, hence, in a shortening of the vibrational progression in RIXS of liquid methanol (Fig. 13). The fine structure seen in the simulated gas phase RIXS profile (Fig. 5) is washed out in the liquid phase (Fig. 13) due to the broadening of the vibrational resonances by much weaker fluctuation of the OH potential in the inner region.

Let us turn our attention to the split $2a''$ RIXS peak discussed in Sec. IV C. A similar splitting, observed in the RIXS spectra of liquid methanol,[15] has been debated. There are two distinct interpretations of the origin of this splitting—a dynamical[15] and a structural interpretation.[75] Both interpretations use a model based on double-well potentials for core-excited and final states[76] which are applicable only for the Rydberg core-excitation or core-ionization of the methanol-dimer. Here, we focus only on the pre-edge core-excitation to the dissociative state which we studied in Sec. IV C for the gas phase. As one can see from Fig. 9, the main contribution to

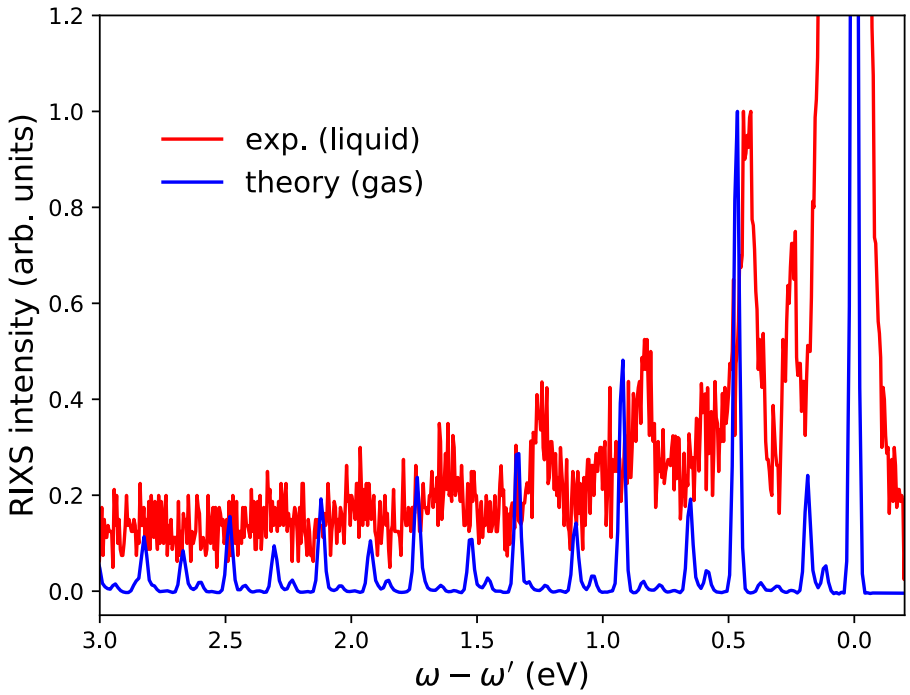

FIG. 13. Comparison of experimental RIXS of liquid methanol with the theoretical multimode RIXS profile of gas phase methanol from Fig. 5. The deviation of the theoretical (gas) vibrational progression from the experimental one (liquid) is due to two reasons. The first one is the intrinsic difference of vibrations in gas and liquid, while the second one is the limitation of the theoretical model used. The photon frequency was tuned in the experiment in the pre-edge region $\omega = 534.5$ eV.

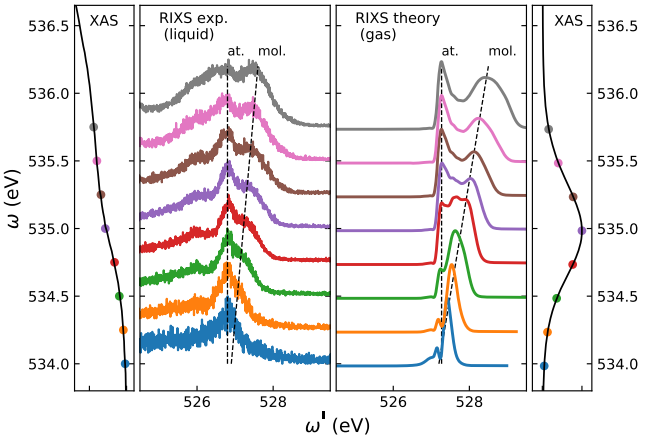

FIG. 14. Comparison of the excitation energy dependence of the experimental RIXS of liquid methanol with the theoretical single-mode RIXS profile of gas phase methanol in the region of the $2a''$ peak (see Fig. 10 for the whole RIXS map). Both liquid and gas phase spectra display nondispersive character of the pseudo-atomic peak and Raman dispersion of the molecular band. The colored circles show the correspondence of the RIXS profile and the excitation energy ω.

the region around the $2a''$ RIXS band comes from the RIXS to the dissociative valence $|2a''^{-1}8a'^{1}\rangle$ excited state. As already explained in Sec. IV C (see also Fig. 8), the formation of the split $2a''$ peak comes from the decay transitions in core-excited CH_3OH in the range rather close to the equilibrium $Q - Q_0 \lesssim 1$ a.u., where the role of the hydrogen bond network is expected to be weak, similar to liquid water.[4] Here, it is important to remember that the nonbonding $2a''$ orbital is rather similar to the nonbonding $1s_O$ orbital (see also Sec. IV D). Akin to the $1b_1 \rightarrow 1s_O$ transition in liquid water, the parallelism of the potentials of the $|2a''^{-1}8a''\rangle$ and $|1s_O^{-1}8a''\rangle$ states is preserved even for longer distances, $Q - Q_0 \gtrsim 1$ a.u.[77] This clearly shows that the nature of the splitting of the $2a''$ peak in liquid is the same as in gas phase methanol at least for pre-edge core excitation. The same excitation energy dependence of the RIXS of liquid and gas phase methanol, in the region near the pseudo-atomic peak (Fig. 14), is another evidence of the dynamical origin of the splitting of the $2a''$ peak. Indeed, both liquid and gas phase spectra display Raman dispersion of the molecular band contrary to the pseudo-atomic peak whose peak position does not depend on the excitation energy.[28]

The experiment shows a structure on the low energy side of the pseudo-atomic peak which is absent in the theoretical spectrum. This can be due to contributions from other vibrational modes, similar to the RIXS of H_2O,[62] that are ignored in the 1D calculations presented in Fig. 14. The theoretical spectrum shows another interesting feature, seen for $\omega < 534.5$ eV, namely, the gradual transformation of the pseudo-atomic peak into the interference hole.[27,78]

V. CONCLUSIONS

We have presented *ab initio* simulations of the X-ray absorption and the resonant inelastic X-ray scattering spectra of gas phase methanol near the oxygen K-edge taking into account the nuclear degrees of freedom. The electronic transitions are calculated using the ADC(2)-x, RASPT2, and TDDFT methods. The multimode nuclear motion is described in the framework of a "mixed representation," where the dissociative states and highly excited vibrational modes are efficiently treated with a time-dependent wave packet technique, while the remaining active modes are described using Franck-Condon amplitudes. It is found that multimode nuclear dynamics is of crucial importance for explaining the experimental XAS and available RIXS spectra. The computed XAS spectra clearly illustrate the state-specific vibrational broadening. The reason for this is the different shapes of the potential energy surfaces for different electronic states. The dissociation of the methanol molecule along the OH bond in the first core-excited state, similar to gas phase and liquid water,[4,6] results in a long vibrational progression in the case of RIXS to the ground state. The ground and dissociative $|2a''^{-1}8a'^{1}\rangle$ final states have the same dissociation limit. Although both these channels participate in the formation of the pseudo-atomic peak, the main contribution comes from the $|2a''^{-1}8a'^{1}\rangle$ channel. We have found that the reason for the splitting of the $2a''$ RIXS peak is the slight difference in the dissociative potential of core- and valence-excited final states along the OH bond. This explains the dependence of the shape of the split $2a''$ peak on the excitation energy and on the isotopic substitution. We also pay special attention to the polarization dependence of the RIXS profile. The presented *ab initio* simulations quantitatively describe the available XAS[16–18] and RIXS[18] experimental data. We show the dynamical origin of the splitting of the $2a''$ peak in RIXS of liquid methanol at least for pre-edge core excitation.

ACKNOWLEDGMENTS

We acknowledge Emelie Ertan for sharing insights into performing the RASPT2 calculations. This work was supported by the Swedish Research Council (Nos. VR 2015-04510, 2015-03781, 2015-03956, and 2016-03619), the Knut and Alice Wallenberg Foundation (Grant No. KAW-2013.0020), Carl Tryggers Foundation, and within the State Contract of the Ministry of Education and Science of the Russian Federation for Siberian Federal University for Scientific Research in 2017–2019 (Project No. 3.2662.2017). V.V.C. and R.C.C. acknowledge the Conselho Nacional de Desenvolvimento Científico e Tecnológico (No. CNPq 234625/2014-7). A.F. acknowledges support by the European Research Council Advanced Grants 2014 Advanced Investigator Grant No. 669531 EDAX under the Horizon 2020 European Union Framework Program for Research and Innovation. M.O. acknowledges support from the Helmholtz Virtual Institute VI419 "Dynamic Pathways in Multidimensional Landscapes." Numerical simulations were performed on the resources provided by the Swedish National Infrastructure for Computing (SNIC 2018/3-104, 023/07-18). The experimental RIXS data were obtained at the ADRESS beamline of the Swiss Light Source at the Paul Scherrer Institut.

APPENDIX A: POTENTIAL ENERGY CURVES OF INACTIVE MODES

As one can see from Fig. 15, the PECs of core-excited states for the remaining modes ν_2, ν_3, ν_4, ν_9, ν_{10}, and ν_{11} are almost parallel to the ground state PECs. Hence, these modes are deemed essentially inactive and are excluded in our simulations.

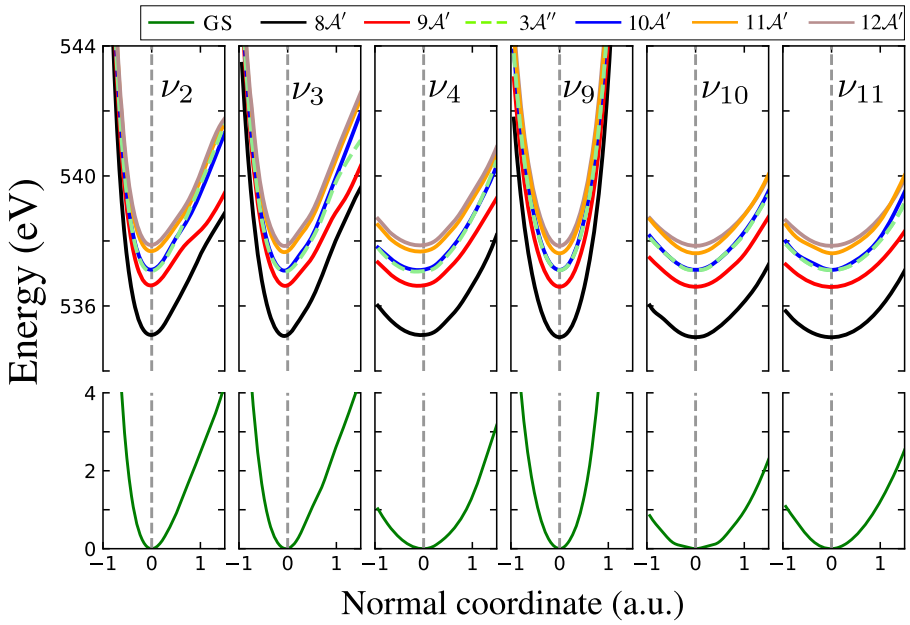

FIG. 15. Potential energy curves for the vibrational modes not taken into account in our simulations. Contrary to the active modes (Fig. 3), those shown in the present figure are not active because the PECs of core-excited states are not significantly shifted with respect to the ground state PECs (green lines).

APPENDIX B: HIGH-LEVEL CALCULATIONS OF THE EXCITED STATES ENERGIES

The calculations of the RIXS spectra for a broad emission energy range (Fig. 12) were performed at the CPP-ADC(2)/aug-cc-pVTZ level of theory, providing a rather good agreement with the experimental spectra[18] at affordable computational costs. However, the energies and thereby the relative peak positions of the valence-excited states may be further improved by using the higher order ADC(3) method and larger basis sets. The energies and oscillator strengths for several lowest valence-excited states computed using different methods and basis sets are collected in Table IV. The same analysis for several lowest core-excited states is presented in Table V. One can see that even though the absolute energies could be worse at the level of ADC(3) as compared to the experimental one, the relative energy difference is improved, e.g., the energy difference between $1A''$ and $3A'$ states is 2.05 eV at the ADC(2)/aug-cc-pVTZ level, while ADC(3)/d-aug-cc-pVTZ provides a value of 1.90 eV, which is closer to the experimental result.

TABLE IV. Valence excitation energies ΔE (eV) and oscillator strength f for methanol, calculated using ADC(2), ADC(2)-x, and ADC(3) methods with Dunning's basis sets: aug-cc-pVTZ (aTZ), d-aug-cc-pVTZ (dTZ), and t-aug-cc-pVTZ (tTZ).[48]

		$1A''$ $2a'' \rightarrow 8a'$		$2A''$ $2a'' \rightarrow 9a'$		$2A'$ $2a'' \rightarrow 3a''$		$3A''$ $2a'' \rightarrow 10a'$		$3A'$ $7a' \rightarrow 8a'$	
		ΔE	$f \times 10^3$	ΔE	$f \times 10^3$	ΔE	$f \times 10^3$	ΔE	$f \times 10^3$	ΔE	$f \times 10^3$
ADC(2)	aTZ	6.48	4.04	7.57	26.93	8.02	28.10	8.15	6.81	8.53	2.85
	dTZ	6.47	3.70	7.55	24.88	7.90	21.28	7.96	5.35	8.52	2.51
	tTZ	6.47	3.70	7.54	24.86	7.90	21.14	7.96	5.42	8.52	2.49
ADC(2)-x	aTZ	6.11	4.08	7.26	26.43	7.77	29.33	7.87	6.52	8.14	2.43
	dTZ	6.10	3.78	7.24	25.02	7.67	23.35	7.72	5.69	8.14	2.33
	tTZ	6.10	3.78	7.24	25.01	7.67	23.25	7.72	5.74	8.14	2.33
ADC(3)	aTZ	7.15	3.43	8.37	38.24	8.95	38.45	8.98	6.41	9.06	0.21
	dTZ	7.15	3.19	8.36	36.35	8.85	30.46	8.84	5.69	9.06	0.21
Expt.[79]		6.67		7.83		...		...		8.43	
Expt.[80]		6.76		7.73		8.31		8.31		...	

TABLE V. Core-valence excitation energies ΔE (eV) and oscillator strength f for oxygen K-edge of methanol, calculated using CVS-ADC(2), CVS-ADC(2)-x, and CVS-ADC(3) methods with Dunning's basis sets aug-cc-pVTZ (aTZ), d-aug-cc-pVTZ (dTZ), and t-aug-cc-pVTZ (tTZ).[48]

	$8\mathscr{A}'$ $1a' \rightarrow 8a'$		$9\mathscr{A}'$ $1a' \rightarrow 9a'$		$3\mathscr{A}''$ $1a' \rightarrow 3a''$		$10\mathscr{A}'$ $1a' \rightarrow 10a'$		$11\mathscr{A}'$ $1a' \rightarrow 11a'$	
	ΔE	$f \times 10^3$	ΔE	$f \times 10^3$	ΔE	$f \times 10^3$	ΔE	$f \times 10^3$	ΔE	$f \times 10^3$
					ADC(2)					
aTZ	534.83	5.36	535.99	1.54	536.37	0.37	536.51	0.37	537.16	2.94
dTZ	534.81	5.31	535.93	1.40	536.17	0.48	536.22	0.46	536.60	1.21
tTZ	534.81	5.31	535.93	1.39	536.17	0.48	536.21	0.45	536.59	1.16
					ADC(2)-x					
aTZ	533.06	8.94	534.85	3.37	535.32	1.02	535.34	3.02	535.93	5.93
dTZ	533.05	8.97	534.82	3.24	535.16	1.27	535.15	2.31	535.68	3.35
tTZ	533.05	8.97	534.82	3.24	535.16	1.26	535.14	2.30	535.67	3.35
					ADC(3)					
aTZ	539.15	20.26	541.24	36.97	542.38	5.11	542.02	7.56	542.69	8.20
dTZ	539.14	20.28	541.23	36.76	542.19	5.23	541.93	6.65	542.52	7.36
tTZ	539.14	20.28	541.23	36.77	542.18	5.22	541.93	6.65	542.52	7.33
Expt.[17]	534.12		535.83		536.32		536.32		537.10	

REFERENCES

[1] P. Norman, K. Ruud, and T. Saue, *Principles and Practices of Molecular Properties: Theory, Modeling, and Simulations* (John Wiley & Sons, Ltd., Chichester, UK, 2018).

[2] S. Schreck, A. Pietzsch, B. Kennedy, C. Såthe, P. S. Miedema, S. Techert, V. N. Strocov, T. Schmitt, F. Hennies, J.-E. Rubensson, and A. Föhlisch, "Ground state potential energy surfaces around selected atoms from resonant inelastic x-ray scattering," Sci. Rep. **6**, 20054 (2016).

[3] S. Eckert, V. Vaz da Cruz, F. Gel'mukhanov, E. Ertan, N. Ignatova, S. Polyutov, R. C. Couto, M. Fondell, M. Dantz, B. Kennedy, T. Schmitt, A. Pietzsch, M. Odelius, and A. Föhlisch, "One-dimensional cuts through multidimensional potential-energy surfaces by tunable x rays," Phys. Rev. A **97**, 053410 (2018).

[4] V. Vaz da Cruz, F. Gel'mukhanov, S. Eckert, M. Iannuzzi, E. Ertan, A. Pietzsch, R. C. Couto, J. Niskanen, M. Fondell, M. Dantz, T. Schmitt, X. Lu, D. McNally, R. M. Jay, V. Kimberg, A. Föhlisch, and M. Odelius, "Probing hydrogen bond strength in liquid water by resonant inelastic x-ray scattering," Nat. Commun. **10**, 1013 (2019).

[5] G. Hura, J. M. Sorenson, R. M. Glaeser, and T. Head-Gordon, "A high-quality x-ray scattering experiment on liquid water at ambient conditions," J. Chem. Phys. **113**, 9140–9148 (2000).

[6] J. Niskanen, M. Fondell, C. J. Sahle, S. Eckert, R. M. Jay, K. Gilmore, A. Pietzsch, M. Dantz, X. Lu, D. McNally, T. Schmitt, V. Vaz da Cruz, V. Kimberg, F. Gel'mukhanov, and A. Föhlisch, "Compatibility of quantitative x-ray spectroscopy with continuous distribution models of water at ambient conditions," Proc. Natl. Acad. Sci. U. S. A. **116**, 4058–4063 (2019).

[7] S. Sarkar and R. N. Joarder, "Molecular clusters and correlations in liquid methanol at room temperature," J. Chem. Phys. **99**, 2032–2039 (1993).

[8] J. A. Morrone and M. E. Tuckerman, "*Ab initio* molecular dynamics study of proton mobility in liquid methanol," J. Chem. Phys. **117**, 4403–4413 (2002).

[9] M. Pagliai, G. Cardini, R. Righini, and V. Schettino, "Hydrogen bond dynamics in liquid methanol," J. Chem. Phys. **119**, 6655–6662 (2003).

[10] G. Cassone, P. V. Giaquinta, F. Saija, and A. M. Saitta, "Liquid methanol under a static electric field," J. Chem. Phys. **142**, 054502 (2015).

[11] T. Weitkamp, J. Neuefeind, H. E. Fisher, and M. D. Zeidler, "Hydrogen bonding in liquid methanol at ambient conditions and at high pressure," Mol. Phys. **98**, 125–134 (2000).

[12] A. H. Narten and A. Habenschuss, "Hydrogen bonding in liquid methanol and ethanol determined by x-ray diffraction," J. Chem. Phys. **80**, 3387–3391 (1984).

[13] S. Kashtanov, A. Augustson, J.-E. Rubensson, J. Nordgren, H. Ågren, J.-H. Guo, and Y. Luo, "Chemical and electronic structures of liquid methanol from x-ray emission spectroscopy and density functional theory," Phys. Rev. B **71**, 104205 (2005).

[14] K. R. Wilson, M. Cavalleri, B. S. Rude, R. D. Schaller, T. Catalano, A. Nilsson, R. J. Saykally, and L. G. M. Pettersson, "X-ray absorption spectroscopy of liquid methanol microjets: Bulk electronic structure and hydrogen bonding network," J. Phys. Chem. B **109**, 10194–10203 (2005).

[15] S. Schreck, A. Pietzsch, K. Kunnus, B. Kennedy, W. Quevedo, P. S. Miedema, P. Wernet, and A. Föhlisch, "Dynamics of the oh group and the electronic structure of liquid alcohols," Struct. Dyn. **1**, 054901 (2014).

[16] A. Hempelmann, M. N. Piancastelli, F. Heiser, O. Gessner, A. Rüdel, and U. Becker, "Resonant photofragmentation of methanol at the carbon and oxygen k-edge by high-resolution ion-yield spectroscopy," J. Phys. B: At., Mol. Opt. Phys. **32**, 2677 (1999).

[17] K. C. Prince, R. Richter, M. de Simone, M. Alagia, and M. Coreno, "Near edge x-ray absorption spectra of some small polyatomic molecules," J. Phys. Chem. A **107**, 1955–1963 (2003).

[18] A. Benkert, F. Meyer, D. Hauschild, M. Blum, W. Yang, R. G. Wilks, M. Bär, F. Reinert, C. Heske, and L. Weinhardt, "Isotope effects in the resonant inelastic soft x-ray scattering maps of gas-phase methanol," J. Phys. Chem. A **120**, 2260–2267 (2016).

[19] B. O. Roos, P. R. Taylor, and P. E. M. Siegbahn, "A complete active space SCF method (CASSCF) using a density-matrix formulated super-CI approach," Chem. Phys. **48**, 157–173 (1980).

[20] J. Finley, P.-Å. Malmqvist, B. O. Roos, and L. Serrano-Andrés, "The multi-state CASPT2 method," Chem. Phys. Lett. **288**, 299–306 (1998).

[21] J. Wenzel, M. Wormit, and A. Dreuw, "Calculating core-level excitations and x-ray absorption spectra of medium-sized closed-shell molecules with the

algebraic-diagrammatic construction scheme for the polarization propagator," J. Comput. Chem. **35**, 1900–1915 (2014).
[22]N. A. Besley, M. J. G. Peach, and D. J. Tozer, "Time-dependent density functional theory calculations of near-edge x-ray absorption fine structure with short-range corrected functionals," Phys. Chem. Chem. Phys. **11**, 10350 (2009).
[23]R. C. Couto, V. Vaz da Cruz, E. Ertan, S. Eckert, M. Fondell, M. Dantz, B. Kennedy, T. Schmitt, A. Pietzsch, F. F. Guimarães, H. Ågren, F. Gel'mukhanov, M. Odelius, V. Kimberg, and A. Föhlisch, "Selective gating to vibrational modes through resonant x-ray scattering," Nat. Commun. **8**, 14165 (2017).
[24]N. Ignatova, V. Vaz da Cruz, R. C. Couto, E. Ertan, A. Zimin, F. F. Guimarães, S. Polyutov, H. Ågren, V. Kimberg, M. Odelius, and F. Gel'mukhanov, "Gradual collapse of nuclear wave functions regulated by frequency tuned x-ray scattering," Sci. Rep. **7**, 43891 (2017).
[25]N. Ignatova, V. Vaz da Cruz, R. C. Couto, E. Ertan, M. Odelius, H. Ågren, F. F. Guimarães, A. Zimin, S. P. Polyutov, F. Gel'mukhanov, and V. Kimberg, "Infrared-pump–x-ray-probe spectroscopy of vibrationally excited molecules," Phys. Rev. A **95**, 042502 (2017).
[26]V. Vaz da Cruz, E. Ertan, R. C. Couto, S. Eckert, M. Fondell, M. Dantz, B. Kennedy, T. Schmitt, A. Pietzsch, F. F. Guimarães, H. Ågren, F. Gel'mukhanov, M. Odelius, A. Föhlisch, and V. Kimberg, "A study of the water molecule using frequency control over nuclear dynamics in resonant x-ray scattering," Phys. Chem. Chem. Phys. **19**, 19573–19589 (2017).
[27]P. Sałek, F. Gel'mukhanov, and H. Ågren, "Wave-packet dynamics of resonant x-ray Raman scattering: Excitation near the Cl L_{II} edge of HCl," Phys. Rev. A **59**, 1147–1159 (1999).
[28]F. Gel'mukhanov and H. Ågren, "Resonant x-ray Raman scattering," Phys. Rep. **312**, 87–330 (1999).
[29]F. Gel'mukhanov and H. Ågren, "Resonant inelastic x-ray scattering with symmetry-selective excitation," Phys. Rev. A **49**, 4378–4389 (1994).
[30]J. Olsen, P. Jørgensen, and J. Simons, "Passing the one-billion limit in full configuration-interaction (FCI) calculations," Chem. Phys. Lett. **169**, 463–472 (1990).
[31]A. D. Becke, "Density-functional thermochemistry. III. The role of exact exchange," J. Chem. Phys. **98**, 5648–5652 (1993).
[32]P. Stephens, F. Devlin, C. Chabalowski, and M. J. Frisch, "*Ab initio* calculation of vibrational absorption and circular dichroism spectra using density functional force fields," J. Phys. Chem. **98**, 11623–11627 (1994).
[33]T. Shimanouchi, "Tables of molecular vibrational frequencies consolidated volume. I," in *Tables of Molecular Vibrational Frequencies Consolidated* (National Bureau of Standards, 1972), Vol. 1.
[34]P.-Å. Malmqvist and B. O. Roos, "The CASSCF state interaction method," Chem. Phys. Lett. **155**, 189–194 (1989).
[35]P.-Å. Malmqvist, B. O. Roos, and B. Schimmelpfennig, "The restricted active space (RAS) state interaction approach with spin-orbit coupling," Chem. Phys. Lett. **357**, 230–240 (2002).
[36]L. S. Cederbaum, W. Domcke, and J. Schirmer, "Many-body theory of core holes," Phys. Rev. A **22**, 206–222 (1980).
[37]A. Barth and L. S. Cederbaum, "Many-body theory of core-valence excitations," Phys. Rev. A **23**, 1038–1061 (1981).
[38]S. Bernadotte, A. J. Atkins, and C. R. Jacob, "Origin-independent calculation of quadrupole intensities in x-ray spectroscopy," J. Chem. Phys. **137**, 204106 (2012).
[39]N. H. List, J. Kauczor, T. Saue, H. J. A. Jensen, and P. Norman, "Beyond the electric-dipole approximation: A formulation and implementation of molecular response theory for the description of absorption of electromagnetic field radiation," J. Chem. Phys. **142**, 244111 (2015).
[40]N. H. List, T. Saue, and P. Norman, "Rotationally averaged linear absorption spectra beyond the electric-dipole approximation," Mol. Phys. **115**, 63–74 (2017).
[41]L. K. Sørensen, R. Lindh, and M. Lundberg, "Gauge origin independence in finite basis sets and perturbation theory," Chem. Phys. Lett. **683**, 536–542 (2017).
[42]P. Norman, "A perspective on nonresonant and resonant electronic response theory for time-dependent molecular properties," Phys. Chem. Chem. Phys. **13**, 20519–20535 (2011).
[43]U. Ekström and P. Norman, "X-ray absorption spectra from the resonant-convergent first-order polarization propagator approach," Phys. Rev. A **74**, 042722 (2006).
[44]U. Ekström, P. Norman, V. Carravetta, and H. Ågren, "Polarization propagator for x-ray spectra," Phys. Rev. Lett. **97**, 143001 (2006).
[45]T. Fahleson, H. Ågren, and P. Norman, "A polarization propagator for nonlinear x-ray spectroscopies," J. Phys. Chem. Lett. **7**, 1991–1995 (2016).
[46]T. Fransson, D. R. Rehn, A. Dreuw, and P. Norman, "Static polarizabilities and C6 dispersion coefficients using the algebraic-diagrammatic construction scheme for the complex polarization propagator," J. Chem. Phys. **146**, 094301 (2017).
[47]D. R. Rehn, A. Dreuw, and P. Norman, "Resonant inelastic x-ray scattering amplitudes and cross sections in the algebraic diagrammatic construction/intermediate state representation (ADC/ISR) approach," J. Chem. Theory Comput. **13**, 5552–5559 (2017).
[48]R. A. Kendall, T. H. Dunning, Jr., and R. J. Harrison, J. Chem. Phys. **96**, 6769 (1992).
[49]M. J. Frisch, G. W. Trucks, H. B. Schlegel, G. E. Scuseria, M. A. Robb, J. R. Cheeseman, G. Scalmani, V. Barone, G. A. Petersson, H. Nakatsuji, X. Li, M. Caricato, A. Marenich, J. Bloino, B. G. Janesko, R. Gomperts, B. Mennucci, H. P. Hratchian, J. V. Ortiz, A. F. Izmaylov, J. L. Sonnenberg, D. Williams-Young, F. Ding, F. Lipparini, F. Egidi, J. Goings, B. Peng, A. Petrone, T. Henderson, D. Ranasinghe, V. G. Zakrzewski, J. Gao, N. Rega, G. Zheng, W. Liang, M. Hada, M. Ehara, K. Toyota, R. Fukuda, J. Hasegawa, M. Ishida, T. Nakajima, Y. Honda, O. Kitao, H. Nakai, T. Vreven, K. Throssell, J. A. Montgomery, J. E. Peralta, Jr., F. Ogliaro, M. Bearpark, J. J. Heyd, E. Brothers, K. N. Kudin, V. N. Staroverov, T. Keith, R. Kobayashi, J. Normand, K. Raghavachari, A. Rendell, J. C. Burant, S. S. Iyengar, J. Tomasi, M. Cossi, J. M. Millam, M. Klene, C. Adamo, R. Cammi, J. W. Ochterski, R. L. Martin, K. Morokuma, O. Farkas, J. B. Foresman, and D. J. Fox, GAUSSIAN 09, Revision A.02, Gaussian, Inc., Wallingford, CT, 2016.
[50]B. O. Roos, R. Lindh, P.-Å. Malmqvist, V. Veryazov, and P.-O. Widmark, "Main group atoms and dimers studied with a new relativistic ANO basis set," J. Phys. Chem. A **108**, 2851–2858 (2004).
[51]F. Aquilante, J. Autschbach, R. K. Carlson, L. F. Chibotaru, M. G. Delcey, L. De Vico, I. F. Galván, N. Ferré, L. M. Frutos, L. Gagliardi, M. Garavelli, A. Giussani, C. E. Hoyer, G. Li Manni, H. Lischka, D. Ma, P.-Å. Malmqvist, T. Müller, A. Nenov, M. Olivucci, T. B. Pedersen, D. Peng, F. Plasser, B. Pritchard, M. Reiher, I. Rivalta, I. Schapiro, J. Segarra-Martí, M. Stenrup, D. G. Truhlar, L. Ungur, A. Valentini, S. Vancoillie, V. Veryazov, V. P. Vysotskiy, O. Weingart, F. Zapata, and R. Lindh, "MOLCAS 8: New capabilities for multiconfigurational quantum chemical calculations across the periodic table," J. Comput. Chem. **37**, 506–541 (2016).
[52]P.-Å. Malmqvist, A. Rendell, and B. O. Roos, J. Phys. Chem. **94**, 5477 (1990).
[53]P.-Å. Malmqvist, K. Pierloot, A. R. M. Shahi, C. J. Cramer, and L. Gagliardi, "The restricted active space followed by second-order perturbation theory method: Theory and application to the study of CuO_2 and Cu_2O_2 systems," J. Chem. Phys. **128**, 204109 (2008).
[54]N. Douglas and N. M. Kroll, "Quantum electrodynamical corrections to fine-structure of helium," Ann. Phys. **82**, 89–155 (1974).
[55]B. Hess, "Relativistic electronic-structure calculations employing a 2-component no-pair formalism with external-field projection operators," Phys. Rev. A **33**, 3742–3748 (1986).
[56]M. Guo, L. K. Sørensen, M. G. Delcey, R. V. Pinjari, and M. Lundberg, "Simulations of iron K pre-edge x-ray absorption spectra using the restricted active space method," Phys. Chem. Chem. Phys. **18**, 3250–3259 (2016).
[57]Y. Shao, Z. Gan, E. Epifanovsky, A. T. B. Gilbert, M. Wormit, J. Kussmann, A. W. Lange, A. Behn, J. Deng, X. Feng, D. Ghosh, M. Goldey, P. R. Horn, L. D. Jacobson, I. Kaliman, R. Z. Khaliullin, T. Kús, A. Landau, J. Liu, E. I. Proynov, Y. M. Rhee, R. M. Richard, M. A. Rohrdanz, R. P. Steele, E. J. Sundstrom, H. L. Woodcock III, P. M. Zimmerman, D. Zuev, B. Albrecht, E. Alguire, B. Austin, G. J. O. Beran, Y. A. Bernard, E. Berquist, K. Brandhorst, K. B. Bravaya, S. T. Brown, D. Casanova, C.-M. Chang, Y. Chen, S. H. Chien, K. D. Closser, D. L. Crittenden, M. Diedenhofen, R. A. DiStasio, Jr., H. Dop, A. D. Dutoi, R. G. Edgar, S. Fatehi, L. Fusti-Molnar, A. Ghysels, A. Golubeva-Zadorozhnaya, J. Gomes, M. W. D. Hanson-Heine, P. H. P. Harbach, A. W. Hauser, E. G. Hohenstein, Z. C. Holden, T.-C. Jagau, H. Ji, B. Kaduk, K. Khistyaev, J. Kim, J. Kim, R. A. King, P. Klunzinger, D. Kosenkov, T. Kowalczyk, C. M. Krauter, K. U. Lao, A. Laurent, K. V. Lawler, S. V. Levchenko, C. Y. Lin, F. Liu, E. Livshits, R. C. Lochan, A. Luenser, P. Manohar, S. F. Manzer, S.-P. Mao, N. Mardirossian, A. V. Marenich,

S. A. Maurer, N. J. Mayhall, C. M. Oana, R. Olivares-Amaya, D. P. O'Neill, J. A. Parkhill, T. M. Perrine, R. Peverati, P. A. Pieniazek, A. Prociuk, D. R. Rehn, E. Rosta, N. J. Russ, N. Sergueev, S. M. Sharada, S. Sharmaa, D. W. Small, A. Sodt, T. Stein, D. Stück, Y.-C. Su, A. J. W. Thom, T. Tsuchimochi, L. Vogt, O. Vydrov, T. Wang, M. A. Watson, J. Wenzel, A. White, C. F. Williams, V. Vanovschi, S. Yeganeh, S. R. Yost, Z.-Q. You, I. Y. Zhang, X. Zhang, Y. Zhou, B. R. Brooks, G. K. L. Chan, D. M. Chipman, C. J. Cramer, W. A. Goddard III, M. S. Gordon, W. J. Hehre, A. Klamt, H. F. Schaefer III, M. W. Schmidt, C. D. Sherrill, D. G. Truhlar, A. Warshel, X. Xua, A. Aspuru-Guzik, R. Baer, A. T. Bell, N. A. Besley, J.-D. Chai, A. Dreuw, B. D. Dunietz, T. R. Furlani, S. R. Gwaltney, C.-P. Hsu, Y. Jung, J. Kong, D. S. Lambrecht, W. Liang, C. Ochsenfeld, V. A. Rassolov, L. V. Slipchenko, J. E. Subotnik, T. Van Voorhis, J. M. Herbert, A. I. Krylov, P. M. W. Gill, and M. Head-Gordon, "Advances in molecular quantum chemistry contained in the Q-Chem 4 program package," Mol. Phys. **113**, 184–215 (2015).

[58] M. Valiev, E. Bylaska, N. Govind, K. Kowalski, T. Straatsma, H. V. Dam, D. Wang, J. Nieplocha, E. Apra, T. Windus, and W. de Jong, "NWChem: A comprehensive and scalable open-source solution for large scale molecular simulations," Comput. Phys. Commun. **181**, 1477–1489 (2010).

[59] T. Yanai, D. P. Tew, and N. C. Handy, "A new hybrid exchange-correlation functional using the coulomb-attenuating method (CAM-B3LYP)," Chem. Phys. Lett. **393**, 51 (2004).

[60] R. C. Hilborn, "Einstein coefficients, cross sections, f values, dipole moments, and all that," Am. J. Phys. **50**, 982–986 (1982).

[61] P. Morin and I. Nenner, "Atomic autoionization following very fast dissociation of core-excited HBr," Phys. Rev. Lett. **56**, 1913–1916 (1986).

[62] E. Ertan, V. Savchenko, N. Ignatova, V. Vaz da Cruz, R. C. Couto, S. Eckert, M. Fondell, M. Dantz, B. Kennedy, T. Schmitt, A. Pietzsch, A. Föhlisch, F. Gel'mukhanov, M. Odelius, and V. Kimberg, "Ultrafast dissociation features in RIXS spectra of the water molecule," Phys. Chem. Chem. Phys. **20**, 14384 (2018).

[63] F. Gel'mukhanov, P. Sałek, T. Privalov, and H. Ågren, "Duration of x-ray Raman scattering," Phys. Rev. A **59**, 380–389 (1999).

[64] F. Gel'mukhanov, T. Privalov, and H. Ågren, "Collapse of vibrational structure in spectra of resonant x-ray Raman scattering," Phys. Rev. A **56**, 256–264 (1997).

[65] S. Sundin, F. Kh. Gel'mukhanov, H. Ågren, S. Osborne, A. Kikas, O. Björneholm, A. Ausmees, and S. Svensson, "Collapse of vibrational structure in the Auger resonant Raman spectrum of CO by frequency detuning," Phys. Rev. Lett. **79**, 1451–1454 (1997).

[66] Y.-P. Sun, Q. Miao, A. Mohammed, H. Ågren, and F. Gel'mukhanov, "Shortening scattering duration by detuning purifies Raman spectra of complex systems," Chem. Phys. Lett. **511**, 16–21 (2011).

[67] A. Pietzsch, Y.-P. Sun, F. Hennies, Z. Rinkevicius, H. O. Karlsson, T. Schmitt, V. N. Strocov, J. Andersson, B. Kennedy, J. Schlappa, A. Föhlisch, J. E. Rubensson, and F. Gel'mukhanov, "Spatial quantum beats in vibrational resonant inelastic soft x-ray scattering at dissociating states in oxygen," Phys. Rev. Lett. **106**, 153004 (2011).

[68] D. R. Yarkony, H. F. Schaefer, and S. Rothenberg, "Geometries of the methoxy radical (X 2E and A 2A1 states) and the methoxide ion," J. Am. Chem. Soc. **96**, 656–659 (1974).

[69] O. Fuchs, M. Zharnikov, L. Weinhardt, M. Blum, M. Weigand, Y. Zubavichus, M. Bär, F. Maier, J. D. Denlinger, C. Heske, M. Grunze, and E. Umbach, "Isotope and temperature effects in liquid water probed by x-ray absorption and resonant x-ray emission spectroscopy," Phys. Rev. Lett. **100**, 027801 (2008).

[70] E. Ertan, V. Kimberg, F. Gel'mukhanov, F. Hennies, J.-E. Rubensson, T. Schmitt, V. N. Strocov, K. Zhou, M. Iannuzzi, A. Föhlisch, M. Odelius, and A. Pietzsch, "Theoretical simulations of oxygen *k*-edge resonant inelastic x-ray scattering of kaolinite," Phys. Rev. B **95**, 144301 (2017).

[71] Y. Harada, T. Tokushima, Y. Horikawa, O. Takahashi, H. Niwa, M. Kobayashi, M. Oshima, Y. Senba, H. Ohashi, K. T. Wikfeldt, A. Nilsson, L. G. M. Pettersson, and S. Shin, "Selective probing of the OH or OD stretch vibration in liquid water using resonant inelastic soft-x-ray scattering," Phys. Rev. Lett. **111**, 193001 (2013).

[72] V. N. Strocov, T. Schmitt, U. Flechsig, T. Schmidt, A. Imhof, Q. Chen, J. Raabe, R. Betemps, D. Zimoch, J. Krempasky, X. Wang, M. Grioni, A. Piazzalunga, and L. Patthey, "High-resolution soft x-ray beamline ADRESS at the Swiss light source for resonant inelastic x-ray scattering and angle-resolved photoelectron spectroscopies," J. Synchrotron Radiat. **17**, 631–643 (2010).

[73] G. Ghiringhelli, A. Piazzalunga, C. Dallera, G. Trezzi, L. Braicovich, T. Schmitt, V. N. Strocov, R. Betemps, L. Patthey, X. Wang, and M. Grioni, "SAXES, a high resolution spectrometer for resonant x-ray emission in the 400–1600 eV energy range," Rev. Sci. Instrum. **77**, 113108 (2006).

[74] F. Hennies, A. Pietzsch, M. Berglund, A. Föhlisch, T. Schmitt, V. Strocov, H. O. Karlsson, J. Andersson, and J.-E. Rubensson, "Resonant inelastic scattering spectra of free molecules with vibrational resolution," Phys. Rev. Lett. **104**, 193002 (2010).

[75] M. P. Ljungberg, I. Zhovtobriukh, O. Takahashi, and L. G. M. Pettersson, "Core-hole-induced dynamical effects in the x-ray emission spectrum of liquid methanol," J. Chem. Phys. **146**, 134506 (2017).

[76] V. C. Felicíssimo, F. F. Guimarães, F. Gel'mukhanov, A. Cesar, and H. Agren, "The principles of infrared-x-ray pump-probe spectroscopy. Applications on proton transfer in core-ionized water dimers," J. Chem. Phys. **122**, 094319 (2005).

[77] M. Odelius, "Molecular dynamics simulations of fine structure in oxygen *k*-edge x-ray emission spectra of liquid water and ice," Phys. Rev. B **79**, 144204 (2009).

[78] R. Feifel, F. Burmeister, P. Sałek, M. N. Piancastelli, M. Bässler, S. L. Sorensen, C. Miron, H. Wang, I. Hjelte, O. Björneholm, A. Naves de Brito, F. K. Gel'mukhanov, H. Ågren, and S. Svensson, "Observation of a continuum-continuum interference hole in ultrafast dissociating core-excited molecules," Phys. Rev. Lett. **85**, 3133–3136 (2000).

[79] T. Yoshidome, H. Kawazumi, and T. Ogawa, "Electron energy-loss spectra of methanol and assignments of its triplet states," J. Electron Spectrosc. Relat. Phenom. **53**, 185–192 (1990).

[80] B.-M. Cheng, M. Bahou, W.-C. Chen, C.-h. Yui, Y.-P. Lee, and L. C. Lee, "Experimental and theoretical studies on vacuum ultraviolet absorption cross sections and photodissociation of CH_3OH, CH_3OD, CD_3OH, and CD_3OD," J. Chem. Phys. **117**, 1633–1640 (2002).